Numerical Analysis of a High Velocity Oxygen Fuel (HVOF) Process

Srivatsan Vengeepuram Rajagopalan

A thesis

in

The Department

of

Mechanical and Industrial Engineering

Presented in Partial Fulfillment of the Requirements
For the degree of Master of Applied Science (Mechanical Engineering) at
Concordia University,
Montreal, Quebec, Canada.

August, 2007

Your file Votre référence
ISBN: 978-0-494-34784-3
Our file Notre référence
ISBN: 978-0-494-34784-3

ABSTRACT

Numerical Analysis of a High Velocity Oxygen Fuel (HVOF) Process

Srivatsan Vengeepuram Rajagopalan

The HVOF process is used for coating protective layers on surfaces exposed to corrosion and wear. This process involves a supersonic two-phase flow of gas-solid particles. The main objective of this thesis is to explore certain key factors that influence the process efficiency such as gas-particle interactions, particle in-flight conditions, and particle loading.

To study the effect of gas-particles interactions, a Lagrangian approach which tracks individual particles in the continuous gas, is used. The supersonic gas flow leaving an HVOF nozzle is over-expanded and its adjustment to the atmospheric pressure results in shock diamonds formation, while flow impingement on a substrate results in bow-shock development. Both the shocks are responsible for affecting the particle conditions. The strength and location of bow shock vary for different substrate geometries and stand-off distances. In this work, various particle sizes impinging on different substrate configurations are simulated and the particle interactions with both the shocks are presented in detail.

To find the effect of particle loading on the gas phase, a dense particulate phase scenario is assumed. A fully Eulerian approach, which treats the particles as a fluid, is used to simulate the HVOF process and the two-phase flow characteristics were investigated for various particle loadings. The particulate phase was found to be dense near the nozzle centerline and dilute near the wall. In the particle-dense region, the gas phase characteristics were found to be severely affected, which significantly affects the particle velocity.

ACKNOWLEDGEMENT

विशुद्ध विज्ञान घन स्वरूपं विज्ञान विश्राणन बद्ध दीक्षम्।
दयानिधिं देहभृतां शरण्यं देवं हयग्रीवम् अहं प्रपद्ये ॥

I profusely thank the Almighty, Lord Sri Krishna, for the blessings that he has been showering upon me. My salutations and first gratitude goes to Him. Second, I bow in respect and love for my Parents, without whom I would not have been anything that I am today. Equivalent to the second, I thank my supervisor Dr. Ali Dolatabadi for his wonderful supervision. I learnt a lot from him, be it the art of presentation or art of being considerate and kind. But for him, nobody would have tolerated my mistakes (some of which are very irritating even to me!). His expert supervision, guidance and timely help, both in terms of academic and personal aspects, are really precious and can't be explained or recognized in few lines. I feel proud and fortunate to be one of his graduate students. I sincerely thank you Dr. Ali! Without you, this thesis would not have come out.

Another very *important* and *special* person to be mentioned here is Ajeetha (my dear life-partner/Saha Dharmini), whose constant encouragement and pestering (well, not always) kept me moving forward, whenever I was stuck. Thanks a lot dear! I also thank my dear sister Srimathi for her prayers and encouragements. Another important person I wish to thank now is my friend and colleague, Mr. Babak A. Samareh. Some of his timely helps are invaluable. I thank you Babak and wish that you reach great heights. I thank all my friends and colleagues for supporting me, in one way or other. Last but not least, my heartfelt thanks to Concordia University and EV building, where I have spent a considerably part of my life, of course happily.

TABLE OF CONTENT

LIST OF FIGURES

LIST OF TABLES

Nomenclature

Latin alphabets

Bi	Biot number
c	turbulent model constant
c_k	speed of sound of material k
c_v	constant volume specific heat
C_D	drag coefficient
d	particle diameter
e	internal energy
E	total energy
g	gravity
H	total enthalpy
k	turbulent kinetic energy
K_{k-l}	inter-phase momentum exchange coefficient
P	production rate of turbulent kinetic energy
R	universal gas constant
Re	Reynolds number
R_{k-l}	inter-phase heat exchange coefficient
S	source term
St	Stokes number
T	temperature
u,v,w	velocity components in x,y, z directions
$\vec{U}$	velocity vector

U_{rel} relative velocity between gas and particels

V volume

Greek symbols

α_k volume fraction of the material k

δ_{ij} Kronecker delta

ε rate of dissipation of turbulent energy

Γ diffusion coefficient

λ thermal conductivity

μ molecular viscosity

μ_{eff} effective viscosity

ρ density

θ_k expected volume fraction of material k

σ turbulent model constant

τ_F fluid time characteristic

τ_R particle response time

Subscripts and Superscripts

BK back cell face

FR front cell face

g gas

k	turbulent kinetic energy
$\mathbf{k}$	particle material
o	pure material
L	left cell face
p	particle
R	right cell face
t	turbulent
c	cell-centered quantity
e	edge location
f	face-centered quantity
n	current time step

1. Introduction

1.1. Overview of Two-Phase Flows of Gas-Solid Particles

The simultaneous flow of solid particles or droplets in a fluid stream is termed as two-phase flow. Two-phase flows are encountered in a large range of flow configurations such as bubbly flows, gas-particle flows and gas-droplets flows. Two phase flows occur in many natural as well as technological scenarios. An example of two phase flow in a natural scenario is the presence of particulate pollutants in the form of dusts, which sometimes have significant impact on the environment flows and heat transfer phenomena. Depending on the concentration of these pollutants, they can affect the solar radiation reaching the earth, thereby changing the heat transfer phenomenon in the atmosphere and thus the flow fields [1].

An example of a two phase flow in a technological scenario is propulsion system in a

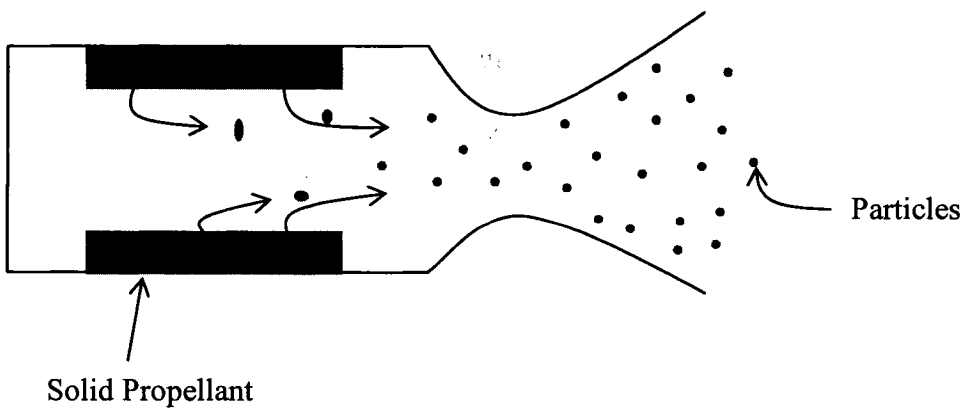

Figure 1.1: Multi-phase flow in rocket combustion chamber

rocket engine, which involves a gas-particle two phase flow. The fuel which is solid propellant is usually aluminum powder. When aluminum burns, small alumina droplets (see *Figure 1.1*), about one micron in size are produced and convected out of the nozzle along with the exhaust gases, resulting in a two-phase flow of gas and solid particles.

1.2. Two Phase Flow in Thermal Spray Process

Thermal spray process is one of the widely used technological systems where two-phase flow phenomena occur. Thermal spray process is used for coating protective layers on surfaces which are exposed to erosion and wear. The process uses thermal energy generated by combustion of fuels or an electric source to heat and accelerate a gas, also called as carrier gas, which is used to deliver the coating particles. The particles exchange momentum and heat with gas, as a result of which attains high velocity and impinges on the substrate at a molten state. Afterwards the particles solidify on the substrate and form a coating. Conventional thermal spray processes are Plasma spray process, Electric wire spray process, High Velocity Oxy-fuel Process (HVOF), Cold Spray process and many more. Micro graphs of coating produced by HVOF and Plasma spray are process are shown in *Figure 1.2a and Figure 1.2b,* respectively. This work concentrates on the study of the HVOF process and investigates some of the critical technological issues that play a role in improving the efficiency of the process. More details about this process is explained in the *Section 1.4,* while following sections will cover some of the major aspects of the physics that governs a two-phase flow.

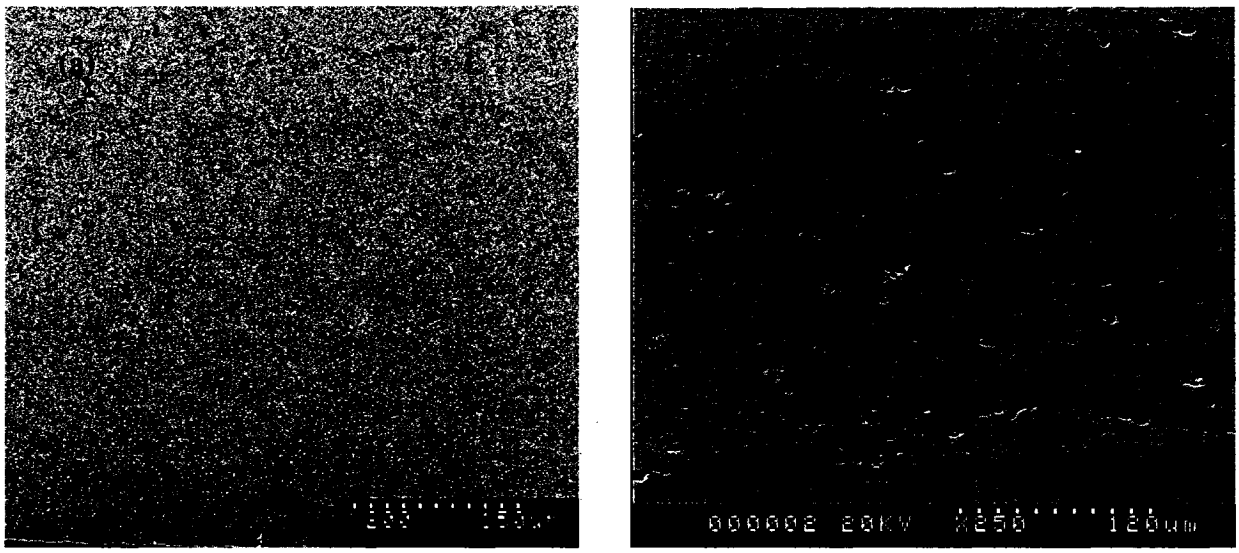

Figure 1.2: Cross section of MCrAlY coating by (a) HVOF process and (b) Plasma process - Courtesy: A. Dolatabadi [37], 2002.

1.3. Physics of Two-phase flows

1.3.1. Dilute Versus Dense Flow

Two-phase flows which involve gas and solid particles can be classified in to two distinct categories, namely, dilute and dense [2]. A dilute flow is one in which the particulate motion is mainly controlled by the fluid forces. On the other hand, in a dense flow inter-particle collision is responsible for characteristics of the particle. A flow can be identified as dilute or dense by comparing the ratio of momentum response time of a particle to the time between collisions. In general, a flow can be qualified as dilute if

$$\frac{\tau_V}{\tau_C} << 1 \qquad (1\text{-}1)$$

where τ_V and τ_c are momentum response time and average time between two successive particle-particle collision, respectively. In this scenario, the particles have sufficient time

to respond to the local fluid dynamic forces before the next collision. If, on the other hand,

$$\frac{\tau_V}{\tau_C} >> 1 \qquad (1\text{-}2)$$

then the particles have no time to respond to the local forces and thus the flow is considered as dense flow [4]. The momentum response time τ_V can be mathematically represented as

$$\tau_V = \frac{\rho_d D^2}{18\mu_c} \qquad (1\text{-}3)$$

Where ρ_d, μ_c and D are density, viscosity and diameter of the particles. In practice there exists is no flow that is perfectly dense or dilute.

1.3.2. Phase Coupling

An important concept in the study of two-phase flows is determining the coupling between the phases. If the presence of dispersed phase has no effect on the continuous phase, a one-way coupling is appropriate to study the physics that governs the two-phase flow. On the other hand if the presence of dispersed phase affects the continuous phase, which normally happens in a dense flow, a two-way coupling is required [3]. Coupling can occur between the two-phases through mass, momentum and energy. Mass coupling is the change in the mass through evaporation or condensation. Momentum coupling is the result of drag between the phases, while energy coupling happens by the heat transfer between the phases.

1.3.3. Scaling Parameters

As mentioned in the previous section, no flow is perfectly dense or dilute as a whole, but either one may give a more descriptive of the physical phenomenon of a specific case. This can be found out by taking into consideration of the certain scaling parameters of the gas-particle flow. One of the important scaling parameters of a two-phase flow is Stokes number, which is the ratio of momentum response time τ_V to a time characteristic of the fluid motion τ_F. It can be mathematically represented as

$$St = \frac{\tau_V}{\tau_F} = \frac{\rho_d D^2 U}{18 \mu_c L} \tag{1-4}$$

where U, L and μ are the fluid velocity, a length characteristic and fluid viscosity, respectively. A low Stokes number ($St<<1$), implies that particles have ample time to respond to the turbulent fluctuations in the flow, which otherwise is called as dilute flow, while a large Stokes number ($St>>1$) implies that the particles are least affected by the carrier gas, but by interaction between then, which implies the flow is dense. Other important scaling parameter is particle volume fraction. Volume fraction (θ), is defined as the ratio of the volume of particle occupied in a control volume to the volume of the control volume. In other words

$$\theta = \frac{\sum V_p}{V} \tag{1-5}$$

1.4. Numerical Approach to Two-phase Flows

Developing a mathematical model for describing a particulate flow has been a challenging issue for researchers in this field, as two-phase flows are too complex to be

treated in a comprehensive way. An ideal model would be something which predicts the properties of the gas phase simultaneously keeping track of the properties of each and every particle in the flow field. Although such constitutive model has not been established at this stage, several available approaches have proved to be useful in predicting some gas-particle flow behaviours, particularly of engineering application. Among them the most common approaches are Lagrangian trajectory approach and Eulerian continuum approach. Both of these methods differ in the way they treat the particle phase in the flow field. Lagrangian approach provides a direct description of particles by calculating the trajectory of each particle i.e. the motion of particles is expressed by an ordinary differential equation in Lagrangian coordinates. A direct integration gives velocity and position of particles in the flow field [3]. This method is appropriate for flows where the mass concentration of particulate phase is low, which corresponds to particle volume fraction less than 10^{-5}.

Another approach that is used to solve a two-phase flow is Eulerian or two-fluid model [4]. In this approach the particle phase is treated as a continuous medium as that of the gas phase. This approach is basically an extension of mathematical formulation of a single-phase to a multi-phase. However, neither of the two phases is actually continuous throughout the flow field, a way to construct continuum of each phase have to be established. The most fundamental step in constructing continuum is selecting an appropriate computational cell. The cell should be large enough in such a way that it contains sufficient particles so that the fluid element has meaningful statistical properties such as density, temperature, mass and velocity. On the other hand, care should be taken

that a computational cell should be small enough compared to the characteristic length of the system so various characteristics of the gas phase can be captured accurately.

1.5. High Velocity Oxygen Fuel Process (HVOF)

After discussing the physics and the numerical models that are associated with a two-phase flow, it is appropriate to discuss about the HVOF process, which is the main objective of this thesis. High Velocity Oxygen Fuel process is one of the widely used coating technology, among the conventional thermal spray processes, due to its relatively low operating temperature, good quality of coating, high bonding strength and reduced thermal stresses [5]. HVOF process involves combustion of a pre-mixed oxygen and propylene inside a specially designed nozzle which is usually a converging diverging nozzle, which burns and accelerates a carrier gas and fine powdered coating material. The combustion process produces temperatures in the range of 2800 K inside thermal spray device, usually accelerates the gas to supersonic velocities, in the divergent section of the nozzle [6]. As a result of this, the injected particles reach high velocities (above 500 m/s),

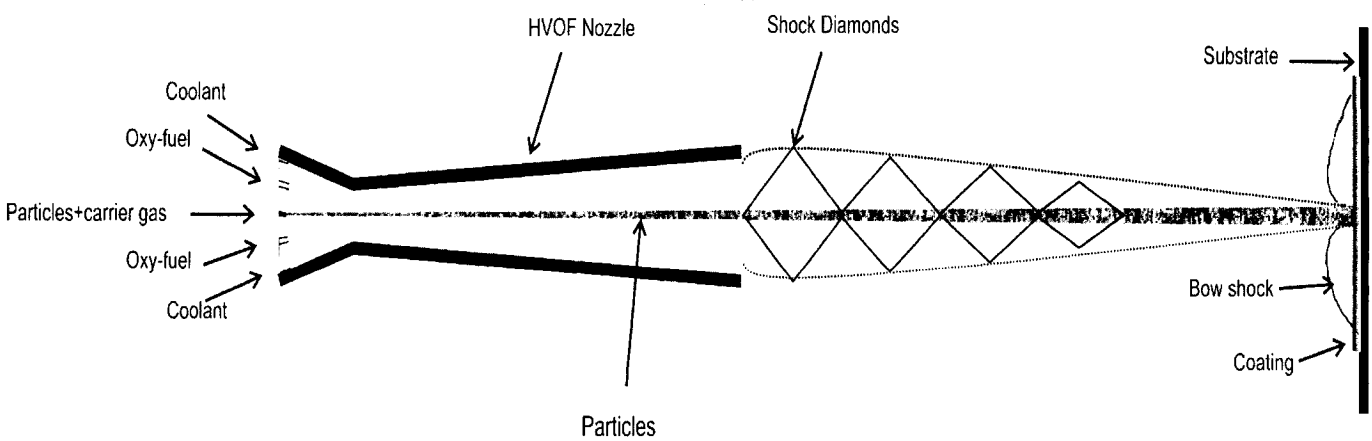

Figure 1.3: Schematic of a High Velocity Oxygen fuel process

depending on their size. High particle kinetic energy upon impact leads to formation of a dense, well adhered coating. Extensive use of this spraying is made in aerospace and power generation industries to provide protective coatings on components that are exposed to heat, corrosion and wear [7]. The schematic of the interior of a typical HVOF nozzle is show in *Figure 1.3*.

As mentioned earlier, the flow is characterized by a release of thermal energy from the combustion of oxy-propylene, which raises the gas pressure to about 5 bars with a temperature 2000 K in the converging section of the nozzle. To protect the nozzle walls normally a coolant gas as shown in *Figure 1.3*, which is usually nitrogen, is also fed into the nozzle. Particles are injected through the central port, with the carrier gas, which is usually nitrogen. The flow of nitrogen also provides enough mass to flow through the nozzle. The high pressure chocks the flow at the throat, which further accelerates through the diverging zone. The flow being over-expanded at the nozzle exit gives raise to a series of expanding and compressing waves in the process of adjusting itself to the atmospheric pressure, called "Shock Diamonds" The resulting supersonic flow decays to subsonic while cool ambient air entrains with the jet [8] [9]. The main objective of this process is to transfer the high kinetic energy of the gases to the particles. The fed particles upon exchange of momentum and energy attain high velocity and temperature and impinge on the substrate. The particles cool down and form a coating on the surface.

1.5.1. Technological Issues

HVOF Process has developed as one of the technological alternative of other conventional thermal spray process, due to its low operating temperature and good

coating quality and yet there are some important issues that have to be studied in order to improve the efficiency and performance of this process. Performance of HVOF process is mainly qualified by a good coating quality, without porosity. Some of the main technological issues that influence the coating quality are discussed below.

Deposition Efficiency

One of the most important characteristics of any thermal spray process is the deposition efficiency (D.E), which is defined as

$$\text{D.E.} = \frac{\textit{Mass of particles deposited on a substrate}}{\textit{Mass of particles fed to the nozzle}} \qquad (1\text{-}6)$$

The deposition efficiency for an HVOF process in practice is not very satisfactory. About 50% of particles fed into the nozzle do not deposit on the substrate. This is due to various reasons. One of the main reasons is the formation of shock diamonds at the nozzle exit. When particles of smaller diameters pass through these shock diamonds, they are deviated from their respective trajectory. *Figure 1.4* shows the deviation of a single

Figure 1.4: Deviation of a particle trajectory due to shock diamonds outside an HVOF nozzle – Courtesy: Ali Dolatabadi [37], 2002.

particle leaving the HVOF nozzle and passing through a shock wave. The landing of these particles and the hence the deposition on the substrate, which is normally kept at a distance of 25 cm far from the nozzle exit is doubted.

Substrate configuration

Placing a substrate, on which the particles should be coated, the high speed flow which will give raise to strong bow shocks or stagnation flows. The stagnation flow may be very strong depending on the location of substrate from the nozzle exit i.e. substrate stand-off distance. This will affect the impact velocity of the particles upon impact [10] [11], in addition to changing their trajectories. The strength of the stagnation flow varies significantly according to the stagnation pressure, which vary with varying geometric configuration of the substrate [12]. Hence optimum substrate stand-off location and favorable substrate configuration will improve the performance of this process.

Particle size and loading

Particle material and size plays an important role in the coating deposition in HVOF process. The presence of shock diamonds outside the nozzle and formation of bow shocks near the substrate will have strong influence on the particle landing conditions depending on the particle size. Smaller particles, due to their relatively lower Stokes number will easily move with the gas phase and any change in the gas phase will affect those particles with smaller size [12]. Particle loading, which is another important parameter that affects the performance of HVOF process, is the ratio of the mass flow rate of the particles to the mass flow rate of the gas phase. It can be mathematically shown as

$$Z = \frac{\Sigma \dot{m}_d}{\Sigma \dot{m}_c} \quad ; \qquad z = \frac{\rho_d u_d}{\rho_c u_c} \tag{1-7}$$

Where Z and z are over-all and local loading, respectively. Local loading is the mass flux ratio at a local flow, while over-all loading is the ratio of over-all mass flow rate of the particulate phase to the over-all mass flow rate of the continuous phase (i.e. gas phase). Particle loading is one of the key issues in deciding whether coupling is required to analyze the two-phase flow or not.

Coating Oxidation

As discussed earlier in *section 1.5*, air from the atmosphere will entrain into the hot supersonic jet, which sometimes oxidizes the particles in-flight. It is necessary to minimize this oxidation of particles in order to achieve a high coating performance. Oxidation of in-flight particles produces metallic oxides which were found to reduce the coating quality [13]. Although in-flight particle oxidation rate is low in a HVOF process, compared to other thermal spray process, ambient air entrainment into the jet should be minimized in order to produce superior coatings.

1.6. Literature Study

High Velocity Oxygen Fuel process involves turbulent, compressible multi-phase reactive flow, with particles. The study of jet flows dates back to 1850's when Helmholtz and Kirchhoff attempted to obtain solution for jet flows. Voluminous literature on jet flows is available which contains a number of established results. However,

computational studies on high speed jet began as early as early 70's by, Dash and Thorpe [14], and Donaldson and Snedekaer [15] [16]. One of the first CFD approach to HVOF process was first conducted by G. D. Power *et al.* [17]. They modeled the flow through the HVOF nozzle, with a powder feeder and studied the flow behavior outside the nozzle. They used two-step finite rate combustion model to model the combustion of propylene. It was assumed that the flow at the nozzle exit had completely mixed and chemical equilibrium has been reached. As the flow chocked at the nozzle exit, they modeled the flow inside and outside the nozzle separately. Therefore the external flow calculations were done only with turbulent mixing with the ambient air. They considered the Lagrangian particle trajectory for modeling the particle behavior.

Oberkampf and Talpallikar [18] [19] modeled an axi-symmetric HVOF problem, considering an Eulerian and Lagrangian formulation for the gas and particles, respectively. They used a one-equation combustion chemistry that accounted for dissociation of combustion products. The used the k-ε turbulence model of Launder and Spalding [20], which is based on Boussineq eddy viscosity concept to model the turbulence. The predicted the relation between the particle size and their response to the gas phase behaviour. Sinha *et al.* [21] simulated HVOF process by a methodology analogous to rocket propulsion and plume impingement.

Yang and Eidelman [22] modeled the TAFA JP gun with a convergent divergent nozzle. They predicted the particle motion in the turbulent flow using Lagrangian Stochastic Model (LSM). In this work particle trajectories and particle temperature were related to

the particle size and distribution. Hassan *et al.* [23] considered the three dimensional geometry of Metco diamond rotating wire torch for simulating HVOF process. They studied the gas dynamics of the process in three dimensional fields. The combustion process is modeled assuming instantaneous chemistry with a one-step chemical reaction. A standard, two-equation, k-ε turbulence model is employed for the turbulent flow field.

Sobolev *et al.* [24] studied the in-flight behavior of stainless steel particles fed through an HVOF gun. They used Lagrangian trajectory method to model the particle motion and studied the mechanical and thermal behavior of the particles. Dolatabadi *et al.* [25] considered the effect of cylindrical shroud attachments to the HVOF spray gun and compared the flow properties with a non-shrouded standard HVOF nozzle. They used an Eulerian formation for gas phase and Lagrangian approach for particle tracking. They used a 4-step eddy dissipation combustion chemistry to model the combustion process that included the dissociation of combustion products.

Dolatabadi *et al.* [26] considered the Eulerian frame for the cloud of particles in the HVOF process. Using Stokes number and particle volume fraction, they evaluated the two-phase flow of gas and solid particle as a dense flow in the nozzle centerline region. They examined the effect of gas phase on the particle using a one-way coupling and their results were experimentally validated [27] [28].

Srivatsan *et al.* [10] and Q. Zhu *et al.* [11] studied the effect of substrate on the flow field and particle impact velocity in the HVOF process and cold spray process, respectively.

Srivatsan and Dolatabadi [29] modeled the HVOF process with different substrate configurations and studied the effect of resulting shock diamonds and bow-shock with the various sizes of particles.

In addition to the above mentioned works in HVOF process, there are many other literatures available which mainly focus on the metallurgy or material properties of the coating particle. There are very few works available which concentrates on the gas dynamics of HVOF, towards improving this process. This thesis intends to concentrate on gas dynamics involved in this process and various technological issues that directly influence the flow properties.

1.7. Objective

The objectives of this thesis include:

- Computationally model a gas-particle flow in an HVOF process using Lagrangian approach and analyze the effect of substrate in the flow field.
- To study the behavior of gas phase and particle conditions due to the change in the substrate configuration.
- Numerically model a two-way coupling between gas and particle using the Eulerian frame work in dense particulate flow situation.
- To find the effect of particle loading on the gas phase properties.

1.8. Thesis Organization

The thesis proceeds as follows. The second chapter presents a detailed description of the Lagrangian approach. The effect of the presence of substrate in the flow field and the flow impingement on the substrate is presented in detail. In addition to this, the effect of substrate geometry on particle trajectories is also discussed in detail. The third chapter presents a description of the Eulerian approach to this problem and the effect of two-way coupling assuming the secondary flow is dense. Finally, the chapter four concludes the work giving a brief note about the future possible extension of this work.

2. Lagrangian Approach

In this chapter, a two-phase flow of gas-particles in a High Velocity Oxygen Fuel (HVOF) process is studied. The Eulerian formulation is used to solve the gas phase, while particle motion is solved by Lagrangian particle tracking method. As discussed earlier in *section 1.2*, Lagrangian particle tracking method treats each particle as a distinct unit and provides a direct description of each particle by tracking their trajectory while simultaneously calculating the respective velocity and mass. The gas phase is treated in an Eulerian frame, with the assumption of continuum.

2.1. Governing Equations

2.1.1. Gas Phase

The gas phase is analyzed by solving continuity, momentum, and energy equations, while the pressure is linked with density through the ideal gas equation. The particle volume fraction is assumed to be negligible, in other words, a dilute flow scenario is assumed. The coupling between the phases is provided by the source terms in the momentum and energy equations. The equations are expressed in the Cartesian tensor form with the Einstein summation convention. The governing equations are as follows.

Continuity Equation

$$\frac{\partial \rho}{\partial t} + \frac{\partial (\rho u_j)}{\partial x_j} = 0 \qquad (2\text{-}1)$$

Momentum Equation

$$\frac{\partial \rho}{\partial t}(\rho u_j)+\frac{\partial}{\partial x_j}(\rho u_j u_i)=-\frac{\partial p}{\partial x_i}+S_{u_i}+\frac{\partial}{\partial x_j}\left\{\mu_{eff}\left(\frac{\partial u_i}{\partial x_j}+\frac{\partial u_j}{\partial x_i}\right)-\frac{2}{3}\mu_{eff}\frac{\partial u_l}{\partial x_j}\delta_{ij}\right\} \tag{2-2}$$

Energy Equation

$$\frac{\partial}{\partial t}(\rho H)+\frac{\partial}{\partial x_j}(\rho u_j H)-\frac{\partial p}{\partial t}=\frac{\partial}{\partial x_j}\left(\lambda\frac{\partial T}{\partial x_j}+\frac{\mu}{\mathrm{Pr}_t}\frac{\partial h}{\partial x_j}\right)+S_E+$$
$$\frac{\partial}{\partial x_j}\left\{u_j\left[\left(\frac{\partial u_i}{\partial x_j}+\frac{\partial u_j}{\partial x_i}\right)-\frac{2}{3}\mu_{eff}\frac{\partial u_l}{\partial x_l}\delta_{ij}\right]+\mu\frac{\partial k}{\partial x_j}\right\} \tag{2-3}$$

Equation of State

$$p=\rho RT \tag{2-4}$$

where $\mu_{eff}=\mu+\mu_t$, H, ($H=h+\frac{1}{2}(u_i u_i)+k$), λ, k, and S are effective viscosity, total enthalpy, thermal conductivity, turbulent kinetic energy and source terms respectively. The standard k-ε turbulence model of Launder and Spalding [20] is where k is the turbulent kinetic energy and ε is the rate of dissipation of turbulent energy. Local values of k and ε are obtained from the solution of the following transport equations:

$$\frac{\partial}{\partial t}(\rho k)+\frac{\partial}{\partial x_j}(\rho u_j k)=\frac{\partial}{\partial x_j}\left(\Gamma_k\frac{\partial k}{\partial x_j}\right)+P_k-\rho\varepsilon \tag{2-5}$$

$$\frac{\partial}{\partial t}(\rho\varepsilon)+\frac{\partial}{\partial x_j}(\rho u_j\varepsilon)=\frac{\partial}{\partial x_j}\left(\Gamma_\varepsilon\frac{\partial k}{\partial x_j}\right)+\frac{\varepsilon}{k}(c_1P_k-\rho c_2\varepsilon) \tag{2-6}$$

The constant values in this model [20] are: $C_\mu = 0.09$; $C_1 = 1.44$; $C_2 = 1.92$; $\sigma_k = 1.0$; $\sigma_\varepsilon = 1.3$. Γ_k and Γ_ε are diffusion coefficients given by $\Gamma_k = \mu + \frac{\mu_t}{\sigma_k}$ and $\Gamma_\varepsilon = \mu + \frac{\mu_t}{\sigma_\varepsilon}$. The production rate of turbulent kinetic energy, P_k is given by:

$$P_k = \mu_t \left(\frac{\partial u_i}{\partial x_j} + \frac{\partial u_j}{\partial x_i} \right) \frac{\partial u_i}{\partial u_j} - \frac{2}{3} \left(\rho k + \mu_t \frac{\partial u_l}{\partial x_l} \right) \frac{\partial u_k}{\partial x_k} \tag{2-7}$$

where μ_t is the eddy viscosity, which is defined as $\mu_t = \rho c_\mu \frac{k^2}{\varepsilon}$, which provides the relation of the turbulence model to the Navier-Stokes energy and reacting flow equations.

Combustion of the oxy-fuel is modeled by a multi-reaction Eddy Dissipation Model (EDM) proposed by Magnussen and Hjertager [30]. The EDM model is appropriate for modeling combustion where the reaction rate kinetics are faster than the turbulent mixing, which means that the reaction in progress is controlled by rate at which the fuel and oxygen is mixed. Experimental observations on HVOF show consensus with using the EDM model. Assuming that air is composed only of N_2 and O_2, the chemistry model involves 6 gaseous species namely, C_3H_6, O_2, CO, H_2, CO_2, H_2O, and N_2.

A three-step chemical reaction is considered to represent the characteristics of the flame which is listed in *Table [2-1]*.The first step in *Table 2-1* describes the fuel cracking; a process that results in hydro carbon intermediates namely, carbon-mono-oxide and hydrogen. The second step describes the oxidation of the carbon-mono-oxide in to carbon-di-oxide and the third step describes the oxidation of hydrogen in to water.

Table 2-1: Combustion Reaction Steps and their Enthalpy of Reaction

Reaction Steps	Chemical Reaction	Enthalpy of combustion (kJ/kg.mol)
1.	$C_3H_6 + \frac{3}{2}O_2 \longrightarrow 3CO + 3H_2$	-3.512 x 10^5
2.	$CO + \frac{1}{2}O_2 \longrightarrow CO_2$	-2.8317 x 10^5
3.	$H_2 + \frac{1}{2}O_2 \longrightarrow H_2O$	-2.4190 x 10^5

The rate of any chemical reaction is decided by either chemical kinetics or the physical mixing of the combusting species. Physical mixing is the process by which the chemical elements get mixed in at molecular levels. A proper atomization leads to the ideal mixing of fuel and oxygen and this mixing is a very crucial parameter for complete combustion and also, the attainment of the required temperature [31]. Chemical kinetics deals with the collision of molecules that change the composition of the gas. Colliding molecules do not retain their identity throughout the duration of the reaction and hence new species are formed at the macroscopic level of the gas [32]. Both of these processes are essential for reactions to occur and either of the two will govern the reaction. The rate determining the process will be the slower one. The mixing rate is determined from the Eddy Dissipation Model (EDM) according to the following expression:

$$R_{k,edm} = -A_{ebu}\rho\frac{\varepsilon}{k}\min\left\{Y_f, \frac{Y_o}{r_k}, B_{ebu}\frac{Y_p}{1+r_f}\right\} \qquad (2\text{-}8)$$

Where,

Y_f = mass fraction of fuel,

Y_o = mass fraction of oxidant,

Y_p = mass fraction of products,

A_{ebu} = EDM model constant,

B_{ebu} = EDM model constant,

r_k = stoichiometry of oxidant,

r_k = stoichiometry of fuel.

The kinetic rate of change of any species in a reaction is given by an Arrhenius expression which is a function of temperature and the concentrations of the reacting chemical species, as expressed in *Equation 2-9:*

$$R_{k,kin} = -A_c T^{\beta} [C_a]^n [C_b]^m \exp\left(-\frac{E_T}{T}\right) \qquad (2\text{-}9)$$

where, A_C = Pre-exponential factor, β = temperature exponent, C_i = Concentration of i^{th} reactant (Kmol/m^3) and E_T = active temperature of the reaction, (K)

2.1.2. Particle Phase

The motion of particles in the flow field is modeled by the Lagrangian Particle Tracking method. The coupling between the gas and the particle phase is provided by the source term in the momentum and energy equations (see *Equations 2-2 and 2-3*). The solid particles are assumed to be non-reactive and spherical in shape. Additionally, due to the small Biot number associated with thermal spray process (i.e. in the order of 10^{-3}) a lumped capacity system in which a uniform temperature distribution is considered with in

each particle is used. The flow that is being considered is assumed to be dilute and hence the volume occupied by the particles is assumed to be negligible. The equation of motion of a single particle in a flow field is defined as follows [33]:

$$m_p \frac{d\vec{U}_p}{dt} = \frac{1}{2}\rho_g A_p C_D \left((\vec{U}_g - \vec{U}_p) \right) \left| \vec{U}_g - \vec{U}_o \right| + \vec{F} \qquad (2\text{-}10)$$

where m_p is the mass of the particle, $\vec{U}_g \; and \; \vec{U}_p$ are velocity of particle and gas, respectively. In this equation, ρ_g is the gas density A_p is the particle cross-sectional area and $\vec{F}$ denotes the external forces acting on the particle. Integrating the equation of motion of the particles (equation *2-10*) over the time interval yields the particle velocity. The gas velocity is assumed to be constant over the integration. A second integration over time gives the particle position at any given time.

Using a lumped capacitance system and neglecting the heat transfer between the phases by radiation, the energy equation of particle can be represented as follows:

$$m_p C_p \frac{dT_p}{dt} = A_p h_c \left(T_g - T_p \right) \qquad (2\text{-}11)$$

In *Equation 2-11,* C_p is the specific heat of the particle at constant pressure and h_c is the convective heat transfer coefficient which can be expressed in terms of the Nusselt number.

$$h_c = \frac{N_u \lambda}{d_p} \qquad (2\text{-}12)$$

The Nusselt number is a function of the Prandtl number and the particle Reynolds number, which is given for a sphere as follows:

$$N_u = 2.0 + 0.6Pr^{0.33}Re_p^{0.5} \tag{2-13}$$

and the particle Reynolds number is a function of the relative velocity between the gas phase and the particle phase, which is given as:

$$Re_p = \rho_g \left| \frac{\vec{U}_g - \vec{U}_p}{\mu_g} \right| d_p \tag{2-14}$$

where d_p is the diameter of particle and μ_g is the viscosity of the gas.

2.1.3. The Dependence of the Drag Coefficient on the Gas Mach Number

Momentum is transferred between the phases through mass transfer and inter-phase drag and lift. In the absence of mass transfer and lift, the drag between the gas phase and particle phase has a predominant role in transferring momentum. The 'steady state' drag is the force that acts on the particle when there is no acceleration on the relative velocity between the particle and the carrier gas and this drag force is quantified by the drag coefficient C_D [33]:

$$F_D = \frac{1}{2}\rho_g A_p C_D \left(\vec{U}_g - \vec{U}_p \right) \left| \vec{U}_g - \vec{U}_p \right| \tag{2-15}$$

where $\vec{U}_g$ *and* $\vec{U}_p$ are velocity of particle and gas, respectively. In this equation, ρ_g is the gas density and A_p is the particle cross-sectional area of the particle.

In general, the drag coefficient C_D depends on many factors such as particle shape, Reynolds number, Mach number, Turbulence, etc. Walsh [34] predicted that the drag coefficient for a particle in a high speed flow will be a function of Reynolds number and Mach number. As the flow under study is supersonic turbulent flow with particles, it is necessary to have a drag coefficient which accounts for all the above mentioned complexities in the flow. *Figure 2.1* shows the variation in the drag coefficient with the particle Mach number at high Reynolds number [3]. The Particle Mach number Ma_p is defined as the ratio of the relative velocity of the gas and particles to the velocity of sound, which is mathematically represented as equation (2-16).

$$M_p = \frac{|U_g - U_p|}{\gamma R T_g} \tag{2-16}$$

It is evident from the figure that at a high Reynolds number the drag coefficient reaches a maximum for transonic flow. This increase is due to the formation of shock waves on the

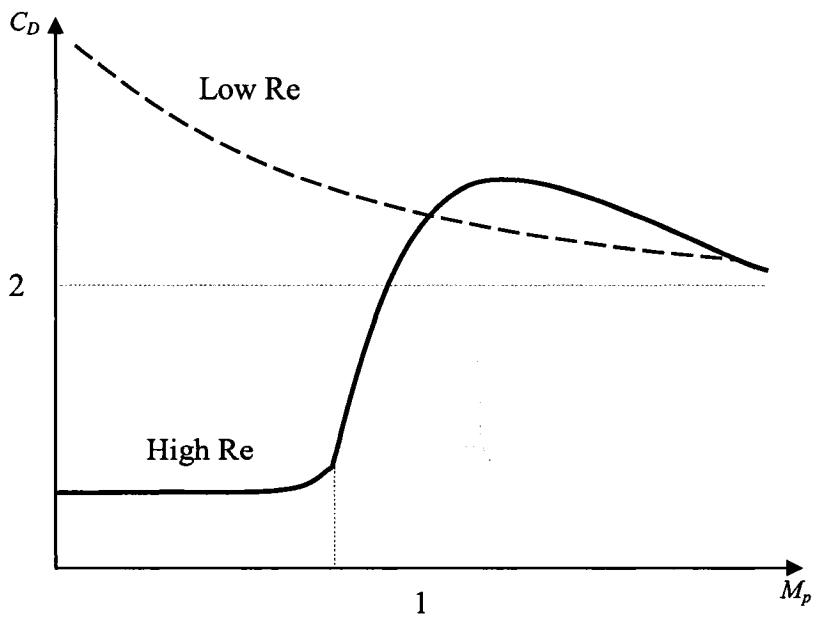

Figure 2.1: Dependence of drag coefficient on Mach number

particle. Mach number effects become significant for a Mach number of 0.6. This is called the critical Mach number wherein a sonic flow occurs in some local region of the sphere.

At a low Reynolds number, the drag coefficient uniformly decreases with increasing Mach number. Also, the trend does not show a high value of C_D near Mach 1. Hence, in order to include this effect of Mach number, we use a C_D correlation that incorporates the effect of Mach number and Reynolds number as suggested by Henderson *et al.* [35], which is shown in *Equation 2-17*. In this equation, Ma , Re, and T are Mach number, Reynolds number and temperature, respectively. The variables with subscript 'p' are that of particles and with subscript 'g' are that of gas, while γ is the specific heat constant of the gas.

$$C_D = \begin{cases} 24\left(\mathrm{Re}_p + (\gamma/2)^{1/2} Ma_p \left\{ 4.33 + \left(\frac{3.65 - 1.53 T_p/T}{1 + 0.353 T_p/T} \right) \exp\left[-0.247 (2/\gamma)^{1/2} \frac{\mathrm{Re}_p}{Ma_p} \right] \right\} \right)^{-1} & \\ + \exp\left(-\frac{0.5 Ma_p}{\mathrm{Re}^{1/2}} \right) \left[\frac{4.5 + 0.38\left(0.03\,\mathrm{Re}_p + 0.48\,\mathrm{Re}_p^{1/2}\right)}{1 + 0.03\,\mathrm{Re}_p + 0.48\,\mathrm{Re}_p^{1/2}} + 0.1 Ma_p^{\,2} + 0.2 Ma_p^{\,8} \right] + & \text{for } Ma_p <= 1 \\ 0.6(\gamma/2)^{1/2} Ma_p \left[1 - \exp\left(-\frac{Ma_p}{\mathrm{Re}_p} \right) \right] & \\ \dfrac{0.9 + \frac{0.34}{Ma_p^{\,2}} + 1.86 \left(\frac{Ma_p}{\mathrm{Re}_p} \right)^{1/2} \left[2 + \frac{4}{\gamma Ma_p^{\,2}} + 1.058 \frac{1}{Ma^p} \left(\frac{2T_p}{\gamma T} \right)^{1/2} - \frac{4}{\gamma^2 Ma_p^{\,4}} \right]}{1 + 1.866 \left(Ma_p / \mathrm{Re}_p \right)^{1.2}} & \text{for } Ma_p >= 1.75 \\ C_D(1.0, \mathrm{Re}_p) + (4/3)(Ma_p - 1)\left[C_D(1.75, \mathrm{Re}_p) - C_D(1.0, \mathrm{Re}_p) \right] & \text{for } 1 < Ma_p < 1.75 \end{cases} \tag{2-17}$$

2.2. Numerical Technique

In this work for analyzing the dilute two-phase flow using Lagrangian method FLUENT™ version 6.1.22 which is a commercial computer program available from ANSYS Inc., U.S.A. [36]. Fluent uses a control-volume-based technique to convert the governing equations to algebraic equations that can be solved simultaneously. This control volume technique consists of integrating the governing equations about each control volume which then yield discrete equations that conserve each quantity on a control-volume basis. The primary variables are velocity components, pressure and temperature. The density is linked with the pressure using the ideal gas law. The governing equations are discretised on quadrilateral control volumes and the cell fluxes are solved using a QUICK scheme. The pressure is coupled with velocity by using a SIMPLE (Semi-Implicit Method for Pressure-Linked Equations) algorithm.

2.2.1. HVOF Nozzle Geometry

The nozzle geometry used in this work is similar to that of DJ -2700 HVOF torch, from Suzler-Metco Inc, Westbury, NY, U.S.A. This torch is basically a converging-diverging nozzle as shown in *Figure 2.2*. The material to be coated is, as fine particles, is fed through the central port along with a carrier gas, which is usually nitrogen. Pre-mixed propylene and oxygen is fed through eight ports of each 1.2 mm, which surrounds the central port concentrically, at an angle of 12^{o} to the centerline. The third stream is nitrogen which serves as coolant to protect the nozzle wall from high temperature. This nitrogen also serves enough mass to push the flow out of the nozzle.

2.2.2. Computational Domain, Mesh and Boundary Conditions

The configuration under study is axi-symmetric and hence one half of the geometry is considered for solving in order to minimize the CPU time. The computational domain is shown in *Figure 2-2*.The domain includes a convergent section, a cylindrical throat followed by a divergent section and a short distance after the nozzle exit is also considered to study the flow pattern outside the nozzle.

In problems involving supersonic flows, the grids need to be more clustered in the axial direction in order to capture shocks and expansion waves accurately. This work uses GAMBIT, version 6.0.2 to generate the geometry and mesh. There are 75 nodes in the radial direction and 96 nodes in the axial direction, inside the nozzle. In order to capture the shock diamonds clearly, fine grids should be used outside the nozzle. A combination of 140 x 200, 160 x 200, 185 x 250, 185 x 300 were used for grid dependency test but, the Mach number was under-estimated and shock diamonds were not captured clearly. It

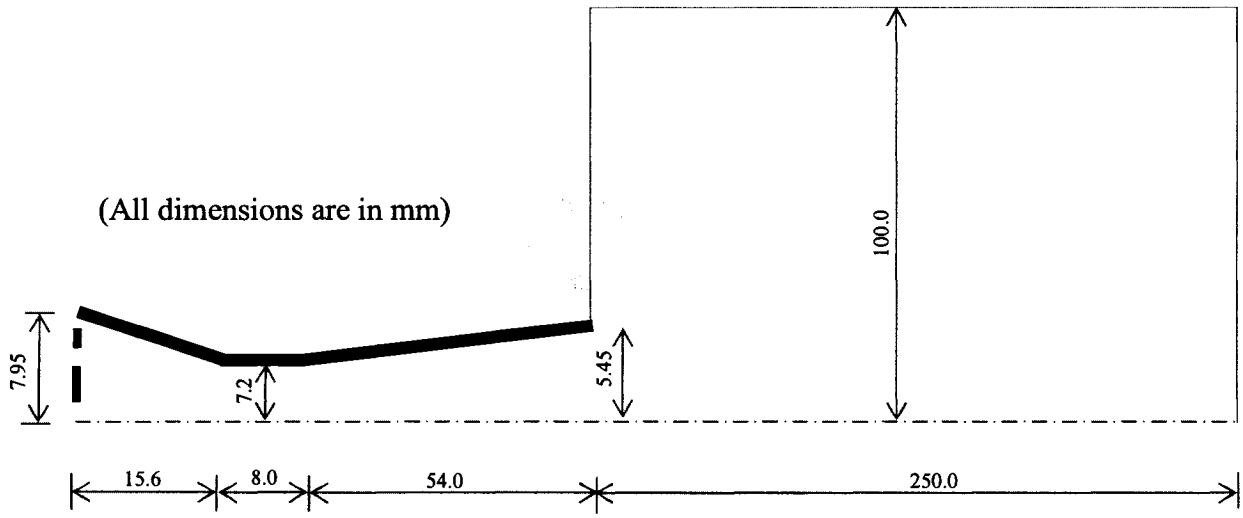

Figure 2-2: Computational domain that is used to model the process

was found that 185 radial nodes and 400 axial nodes, which are highly clustered near the nozzle exit was found to capture the shock diamonds clearly, outside the nozzle. On the high end the extremely clustered combination of 200 x 500 and 250 x 600 were tested, and it was observed that the difference in the Mach number value was less than 0.04 and the normalized temperature was less than 0.005.

The boundary conditions are as shown in *Figure 2-3*. The mass flow rate boundary is assigned to the three inlets, through which the gas, particles and premixed oxy-fuel are injected. The mass flow rate of the species mentioned in *Table 2-2* is in accordance with experiments conducted by Dolatabadi [37], 2002. The injection of gas and particle at inlets are assumed to be 350 K and the walls are assumed to be 320 K. A pressure-far-field boundary condition is applied to the region outside the nozzle where pressure is assumed to be atmospheric.

The High Velocity Oxygen Fuel process is numerically simulated and the results are presented with discussions in the remaining sections of this chapter. The results of the gas

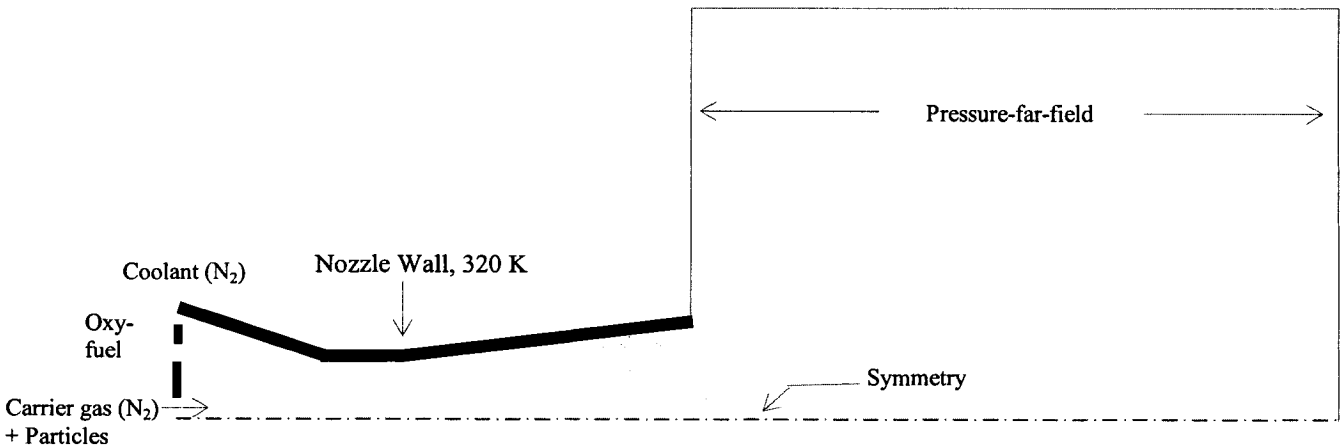

Figure 2-3: Boundary conditions applied

and particle phases are presented separately followed by the discussion about the effects of variations in gas phase characteristics on the particle phase. The topics to be discussed in the following sections include the effect of shock diamonds on particles, the effect of the substrate stand-off distance on particles and finally, the effect of substrate configuration on particles.

Table 2-2: Inlet mass flow rate of different species - Courtesy: A. Dolatabadi [37], 2002

Inlet	Species	Mass Flow Rate (kg/sec)
1	N_2 (Carrier gas)	1.573×10^{-4}
	MCrAlY alloy particles	5.400×10^{-4}
2	C_3H_6 (Fuel)	2.256×10^{-3}
	O_2 (Oxygen)	6.484×10^{-3}
3	N_2 (Coolant)	8.604×10^{-4}

2.3. Results and Discussion

2.3.1. Gas phase

General characteristics of the free jet emerging out of the HVOF nozzle are shown in *Figures 2.4* and *2.5*. In these figures, contours of pressure, temperature and the Mach number are presented. The combustion of oxy propylene raises the gas pressure to around 5 atmospheres and the temperature to around 2800 K at the inlet zone of the nozzle. This is very much evident from *Figure 2.4b*. The flow is accelerated by this pressure rise and reaches Mach 1 at the nozzle throat, as shown in figure 2.5. The flow further accelerates through the divergent section of the nozzle and develops into a supersonic flow.

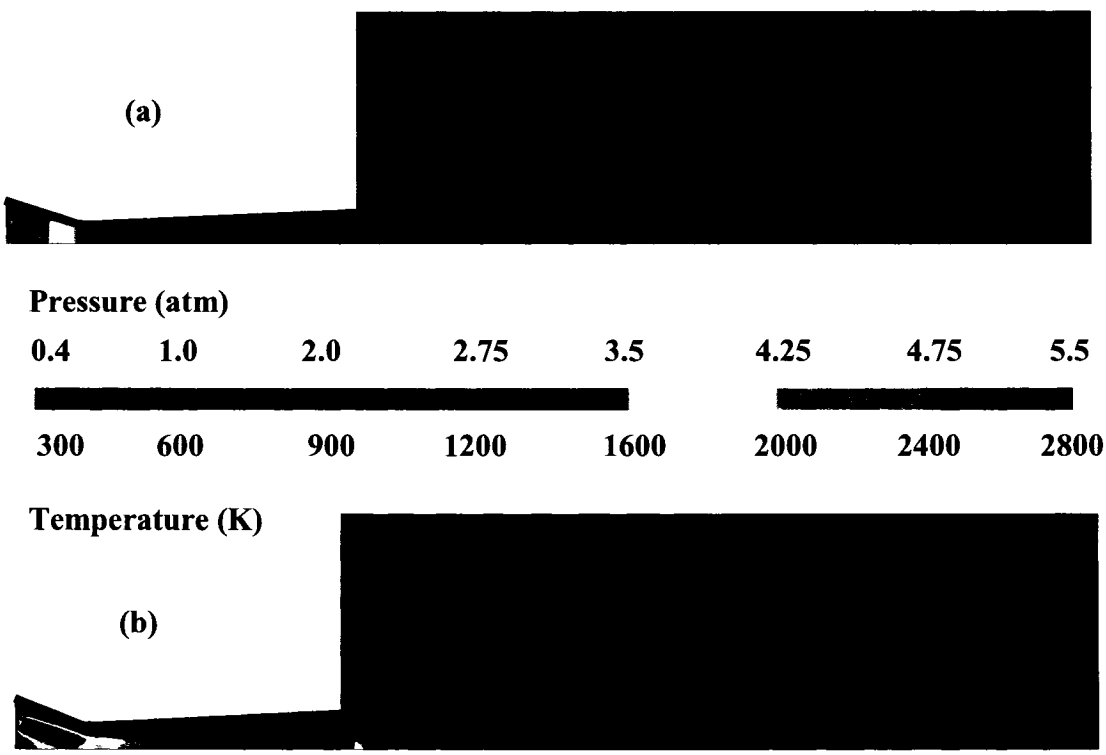

Figure 2.4: Gas phase (a) Pressure contour and (b) Temperature contour

The high speed flow, while expanding through the divergent section of the nozzle, comes out of the nozzle as an over-expanded jet whose Mach number is more than 2.4 and pressure less than the atmospheric pressure. The over expanded flow is compressed suddenly by the surroundings, so that the gas pressure rises more than atmospheric pressure. The gas expands again in order to equalize with atmospheric pressure giving rise to series of compressions and expansions waves the gas finally settles down to the

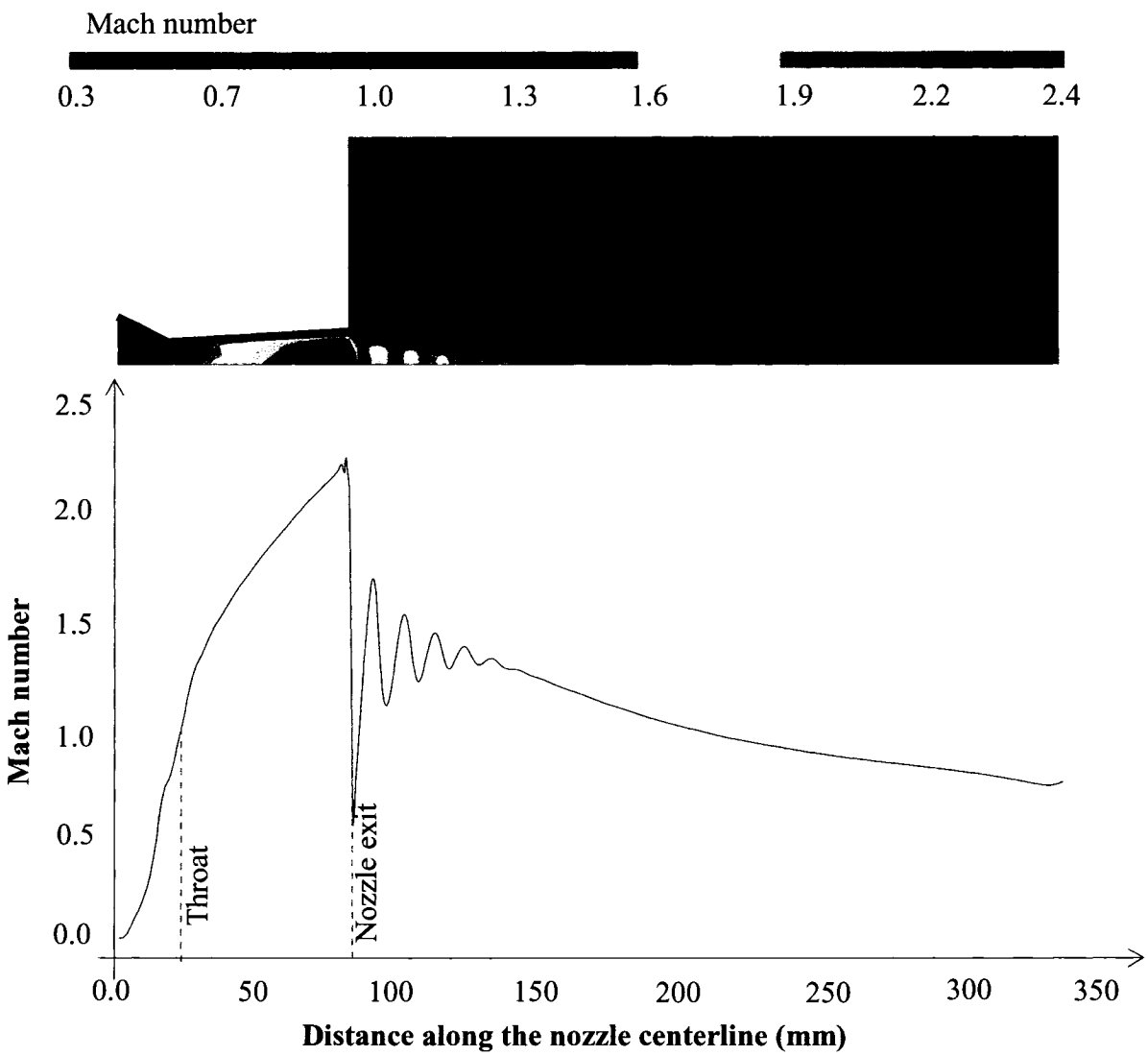

Figure 2.5: Gas phase Mach number along the nozzle centerline

atmospheric pressure. These series of compression and expansion waves are nothing but oblique shocks and Prandtl-Meyer expansion fan, which forms a diamond like pattern. This effect can also be clearly visualized in *Figure 2.6* where absolute pressure along the nozzle centerline is plotted against nozzle axis.

Figure 2.7 shows the axial velocity of the gas along the nozzle centerline plotted against the axial length of the nozzle. The high pressure due to combustion accelerates the gas to around 1800 m/s at the nozzle exit and the shock diamond that is present outside the nozzle exit decelerates the gas abruptly to around 500 m/s and the gas velocity increases again when it passes through the expansion fans and decreases again when it passes through the shock diamonds. In this way, the velocity is alternatively decelerated and accelerated. This effect is also clearly seen when Mach number is plotted against the

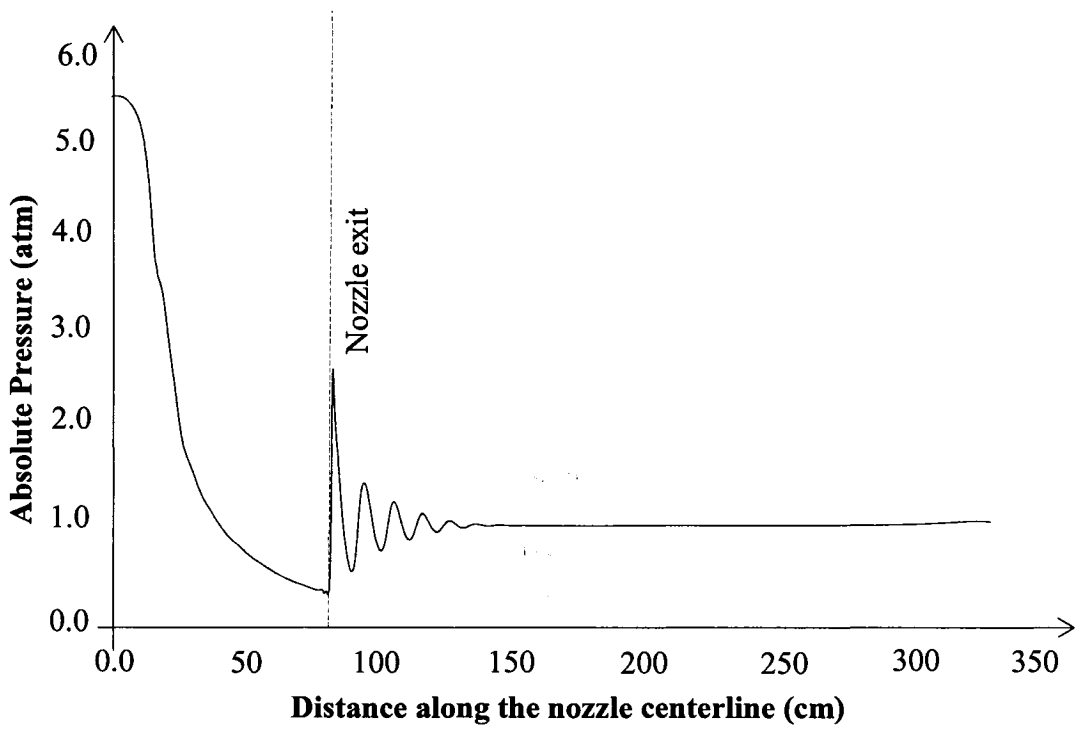

Figure 2.6: Absolute pressure of the gas phase along the nozzle centerline

axial distance, in *Figure 2.7.* It is significant to note that the Mach number is 1 at the throat, while at the exit it is around 2.4. We can also see that the flow after passing through four or possibly five shock waves settles down to a normal jet.

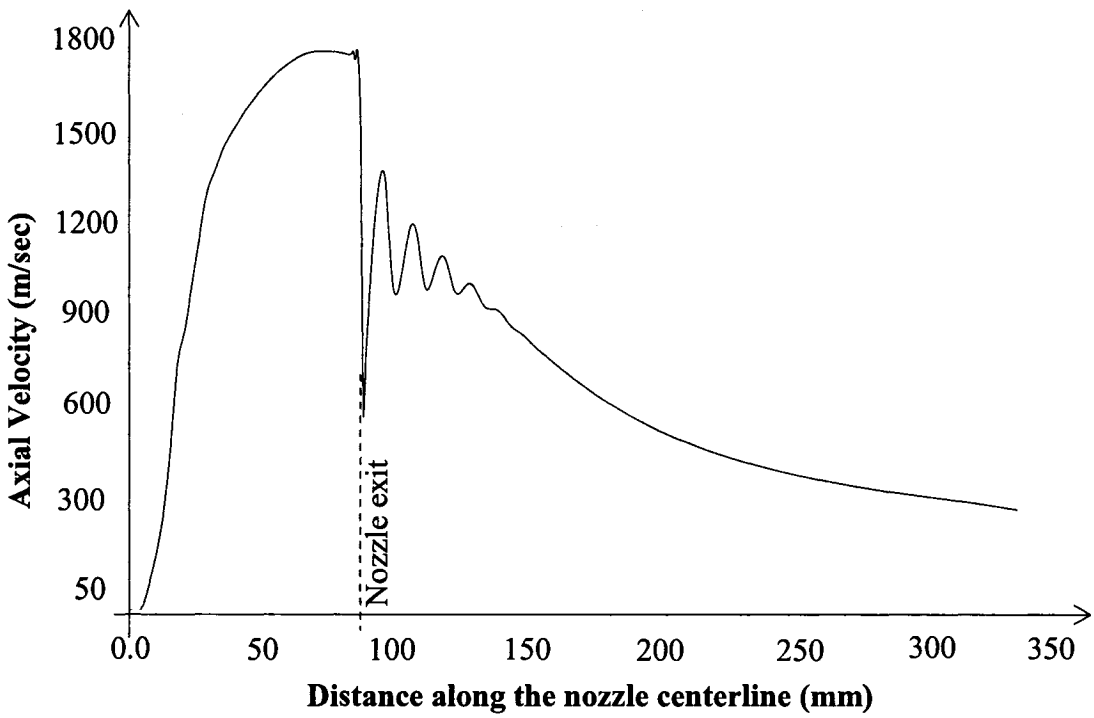

Figure 2.7: Axial velocity of the gas along the nozzle centerline

From *Figures 2.5 and 2.7*, it can be observed that at a distance of 300 mm from the nozzle exit the Mach number and axial velocity of the free jet are about 0.8 and 500 m/s respectively, where a substrate is usually placed. In addition to this, the static temperature of the jet is around 900 K. When a substrate is placed in this flow regime, the high speed flow is decelerated rapidly and this yields a strong reverse flow or stagnation flow. This effect is discussed in detail in the *Sections 2.3.4.*

2.3.2. Particle Phase

The results of particle phase are discussed in this section. The particle trajectories are tracked using Lagrangian stochastic tracking method and the results are presented in *Figures 2.8 and 2.9*. The particle under study is a nickel particle that has a density close to 8500 kg/m^3 and a specific heat of 500 J/kg. K. The sizes of particles under study are 10 and 30 μm. The particle velocity of 10 μm and 30 μm are plotted against the length of the nozzle is shown in *Figures 2.8a* and *2.8b,* respectively. From *Figure 2.8a*, it is evident that the 10 μm particles are swiftly accelerated inside the nozzle due to the large relative velocity between the gas and the particles. Even after the particles exit the nozzle, they continue accelerating due to the expansion waves present at the nozzle exit. These particles start decelerating when they pass through a series of shock diamonds and continue to decelerate further by the turbulent shear layers. Thus, we see that the particles' velocity decreases from around 1300 m/s to 400 m/s over a distance of 0.25 m. In this process, we also observe that the fluctuation in particle velocity is very high due to that they are very small in size and also have a low Stokes number in the order of 10.

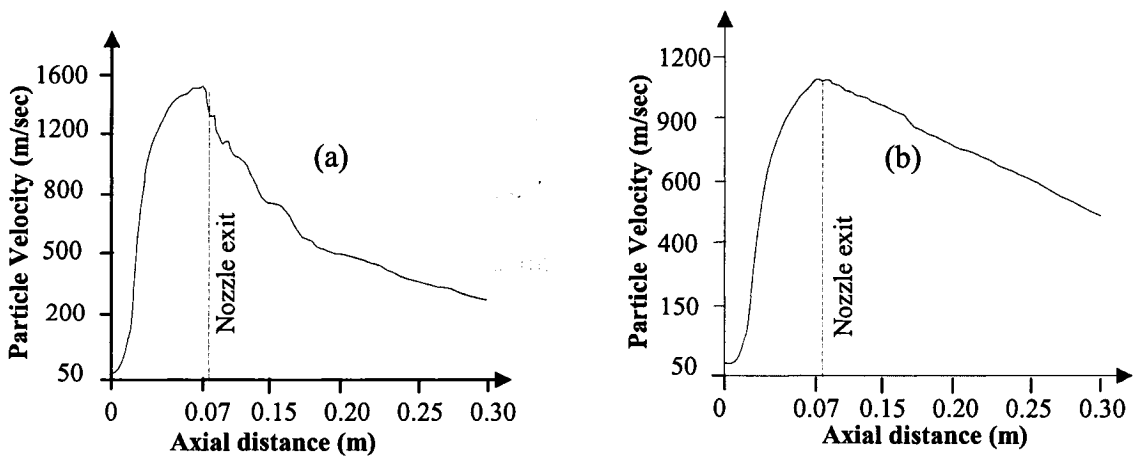

Figure 2.8: Particle velocity of (a) 10 μm and (b) 30 μm particle

Figure 2.8b explains the velocity of the 30 μm particles as it travels through the domain. The initial particle velocity is close to 50 m/s and the particles are accelerated there after. The maximum velocity attained by these particles is slightly more than 1000 m/s and as they pass through the shock diamonds, they are not decelerated as the 10 micron particles are; when they leave the domain their velocity is close to 600 m/sec. This means that there is a 35% reduction in the velocity over a distance of 0.25 m compared to a 65% reduction in velocity for the 30 micron particles. This is due to the large Stokes number which is in the order of 10^2 that is associated with the heavy particles. This number is very large for the particles to respond to the changes in the gas phase.

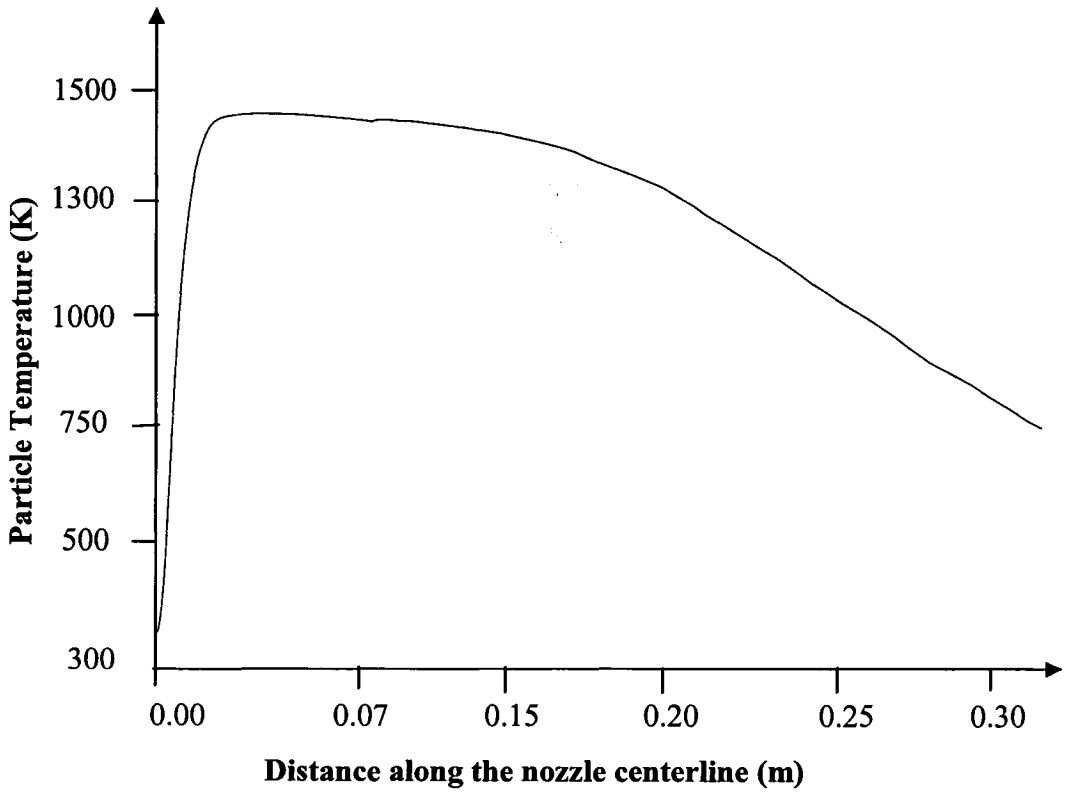

Figure 2.9: Temperature profile of 10 μm particles along the nozzle centerline

Figure 2.9 shows the temperature profile of the 10 μm particles. It is evident from this figure that the particles heat up from the high temperature due to combustion and therefore, the particle temperature rises inside the nozzle and reaches a maximum of around 1500 K at the nozzle exit. There is also additional heating by the thermal shocks.

As the particles travel through the domain, they lose heat due to the entrainment of ambient air and when they reach the end of domain, the particle temperature is around 750 K. This value is less than the experimental values predicted by Dolatabadi *et al.* [25]. A possible reason for this under-prediction may be due to the fact that particle oxidation is not modeled in this simulation. The oxidation of particles is an exothermic process and thus, increases the particle temperature compensates for the heat loss due to ambient air mixing.

2.3.3. The Effects of Shock Diamonds on Particles

Previous section demonstrated that the gas flow is over expanded when it reaches the nozzle exit which results in alternative compression and expanding waves called shock diamonds which finally settles down to atmospheric pressure. These shock diamonds can be clearly seen in *Figures 2.4 and 2.5*. When small particles pass through these sets of compression and expansion waves, they are accelerated and decelerated alternatively, which results in a heavy loss of momentum gained by the particles. In addition to this, the trajectory of the particles is severely affected by the shocks diamonds in their path. This effect has been picturised in *Figure 1.4*. This section is dedicated to studying the effects of these shock diamonds on particle characteristics such as velocity and location. By

comparing the particle conditions before and after shock diamonds, their influence on the particles can be understood clearly. In order to realize this, particle velocity is plotted against respective particle radial position at two different locations; the nozzle exit plane and a location at 250 mm from nozzle exit. The results are shown in *Figure 2.10,* and tabulated in *Table 2.3 and Table 2.4* for 10 and 30 μm, respectively.

Figure 2.10 shows the change in velocity of the 10 μm particles at the nozzle exit plane and at a distance of 250mm from the nozzle exit. Data of 1000 particle were collected; however 250 particles are shown in the figure for clear visualization. From *Figure 2.10a,* it can be seen that all the particles in the radial plane is very close to the nozzle centerline with high velocity. The respective mean values can be learnt from *Table 2.3.* The particle average velocity is around 1300 m/s with a mean radial location 1.2. The respective standard deviations are 20 and 0.8 approximately. When the particles pass through the shock as they come out of the nozzle, they are severely decelerated and scattered by the alternatively expanding and compressing waves. As a result of this, the average velocity of the particles at 250 mm reduces to 320 m/sec with an average radial location shifted to around 7 mm.

Table 2.3: Particle condition of size 10 micron at nozzle exit and at 250 mm from the nozzle exit

Axial distance	**Mean Velocity (m/sec)**	**Std Dev (m/sec)**	**Mean radial location (mm)**	**Std Dev (mm)**
Nozzle exit (0 mm)	1300	19.87	1.20	0.82
At 250 mm	320	48.52	6.8	3.65

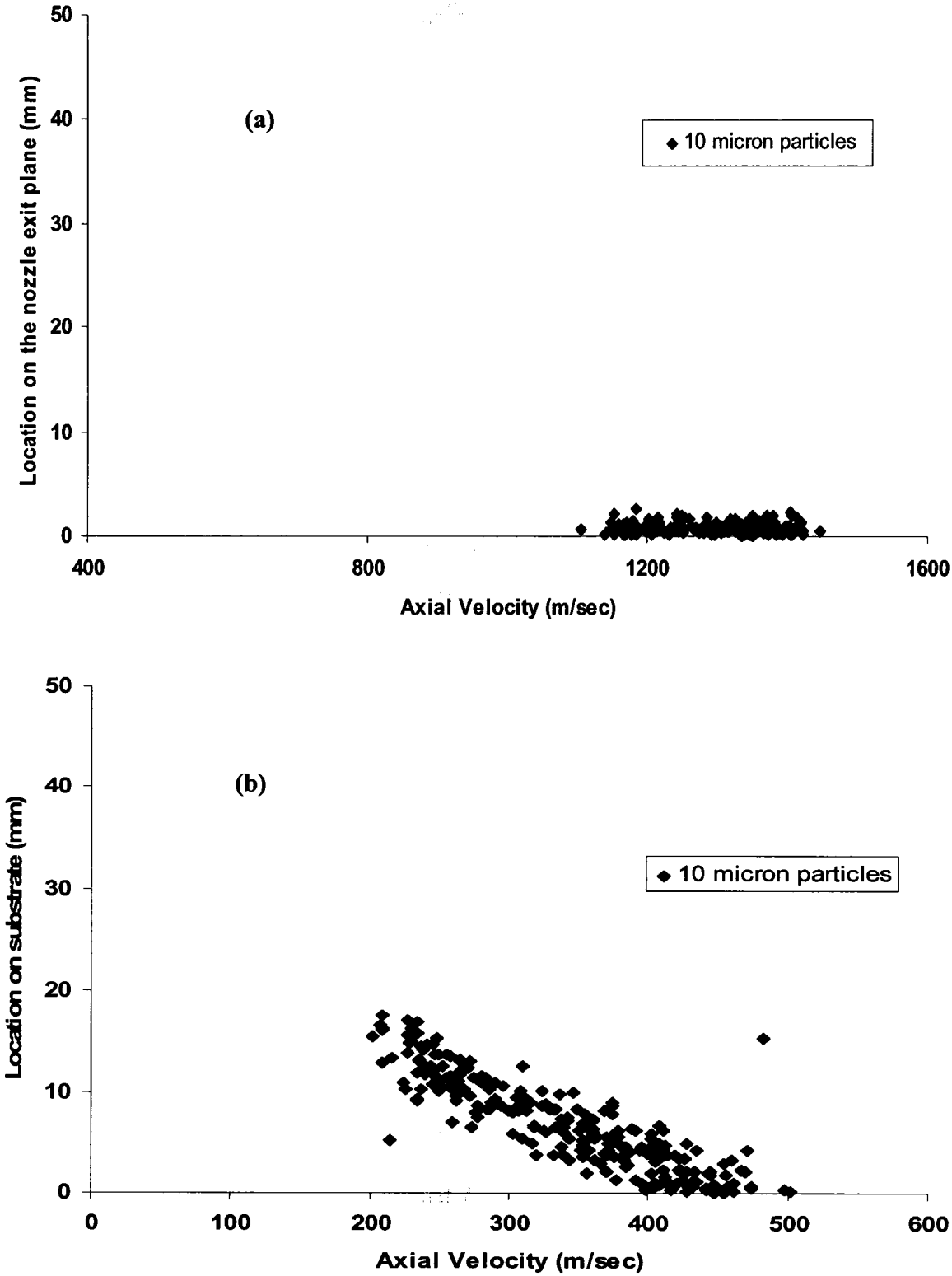

Figure 2.10: Particle conditions of size 10 μm at (a) Nozzle exit plane and (b) A plane at 250mm from nozzle exit

Although particles lose some momentum as they travel through the domain, most of the momentum loss is contributed by the shock diamonds which decelerate the light particles i.e. 10 μm, abruptly but also scatters them away from their normal trajectory. This clearly shown in *Figure 2.10b*, where particle conditions at 250 mm is picturised. It can be seen that particles are widely scattered with reduced mean velocity. This demonstrates the severe effects of shock diamonds on smaller particles. This clearly shows the severe effects of shock diamonds on smaller particles.

The same type of analysis conducted on 30 micron particles did not show a significant difference between the two chosen locations. From *Table 2.4*, it can be seen that the maximum velocity attained by these particles at the nozzle exit is around 950 m/sec with an average radial location of 0.6 mm off the nozzle centerline. At a distance of 250mm from nozzle exit, the average velocity of these particles is close to 600 m/sec with an average radial location from the centerline equal to 3 mm. Therefore, there is a velocity difference of 350 m/sec with a 3 mm shift in the radial location over a distance of 25 cm. Comparing *Table 2.3* and *Table 2.4*, it can be understood that the change in the velocity and trajectory for heavy particle i.e. 30 μm particles, due to the shock diamonds is not

Table 2.4: Particle condition of size 30 micron at nozzle exit and at 250 mm from the nozzle exit

Axial distance	**Mean Velocity (m/sec)**	**Std Dev (m/sec)**	**Mean radial location (mm)**	**Std Dev (mm)**
Nozzle exit (0 mm)	940	5.42	0.60	0.68
At 250 mm	591	12.33	3.27	1.81

significant as compared to the 10 μm particles. In other words 30 μm particle show poor response to the shock diamonds that is present at the nozzle exit. This is due to the large Stokes number associated with heavy particles. As mentioned in the *section 1.1.3*, a large Stokes number implies a large particle response time, which means that 30 μm particles do not respond quickly to the changes in the gas phase and this is the reason why large particles are not affected by the presence of shock diamonds.

2.3.4. The Effects of the Substrate Stand-Off Distance

The presence of an obstruction in the way of a supersonic jet can significantly change the characteristics of the jet near its vicinity. A substrate in the flow field is one such obstruction for the supersonic jet emerging out of an HVOF nozzle. The effects of placing a substrate in the flow field are demonstrated in *Figure 2.11* by comparing the Mach number contours of a free jet and those of an impinging jet. When high speed flow is stopped by a substrate, the flow comes to a stagnation abruptly and gets diverted in to a direction perpendicular to its trajectory, which can be identified by the velocity vector of the gas near the substrate, which is presented in *Figure 2.11*.strong reverse flow occurs and a bow-like formation of the reverse flow appears on the surface of the substrate. This reverse flow is due to sudden flow stagnation of the high speed jet which will henceforth be termed as bow shock. The velocity vector near the substrate is enlarged and presented to show the direction of the flow in this stagnation region. It is illustrated in *Figure 2.11* that when high speed flow hits a substrate, the flow is suddenly decelerated and the flow is diverted in a direction perpendicular to its original direction, which can be seen by the direction of the velocity vector near the substrate.

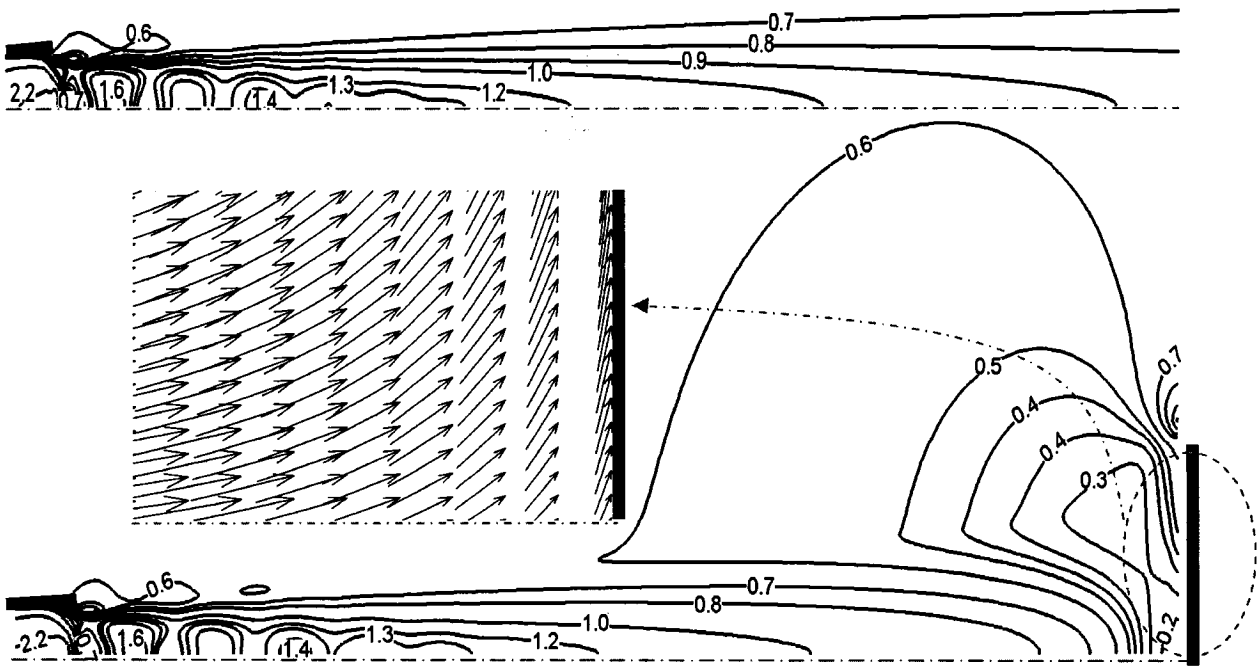

Figure 2.11: Variation of gas phase Mach number, due to the presence of a substrate

The strength and nature of the bow shock varies with the stand-off distance of the substrate. It is predictable that a bow shock formed on a substrate that is kept very close to the nozzle exit will be very strong and the flow reversal caused by this may even interact with the supersonic main jet and with the shock diamonds. This phenomenon drastically affects the flow characteristics of the particles that are flowing along with the jet. Hence, the location of a substrate becomes a key issue in improving the efficiency of the HVOF process. This creates a need to study particle characteristics such as average impact velocity and their landing location on the substrate at various stand-off distances. In order to understand the effects of the substrate stand-off distance on particle characteristics, four different stand-off distances namely, 200, 250, 300 and 350 mm, were studied for four different particle sizes; 1 micron, 10, 30 and 60 μm.

Table 2.5: Variation of particle impact velocity (V_{im}) and landing location (r_L) over the substrate stand-off distances

Stand-off distance (mm)	Mean particle impact velocity (V_{im}) and landing location (r_L) on substrate							
	1 μm		10 μm		30 μm		60 μm	
	V_{im} (m/s)	r_L (mm)	V_{im} (m/s)	r_L (mm)	V_{im} (m/s)	r_L (mm)	V_{im} (m/s)	r_L (mm)
200	112.8	30.4	241.3	11.5	614.6	3.1	644.7	2.1
250	121.2	26.5	258.3	10.1	572.9	3.5	619.7	2.2
300	127.3	25.4	230.8	11.2	534.5	3.8	572.5	2.4
350	101.2	26.2	200.4	12.3	498.3	4.1	546.4	2.7

A total number of 500 particles' data is collected and the results are presented in *Table 2.5* which tabulates the impact velocity of various particles (1 μm, 10 μm, 30 μm and 60 μm) at four different substrate stand-off distances. It is very much evident that the impact velocity of 1 micron particles for all stand-off distances is rather low (around 120 m/s). Although these particles travel with the same velocity as the carrier gas, they are easily affected by the shock diamonds and the turbulent shear layers outside the nozzle. In addition to this, the bow shock decelerates these light particles drastically, shifting their average landing location far from the nozzle centerline. Additionally from *Table 2.5* that the average landing location of these particles is approximately 25 mm away from the nozzle centerline, which implies that up to or more than 50% of particles injected will not even land on the substrate. These small particles travel with almost the same velocity of the gas and due to its very low Stokes number, they are very much sensitive to the

variations in the gas phase characteristics. Due to this, alternating compression and expansion waves of the shocks diamonds and the bow shock near the substrate severely affect the trajectory and the velocity of these particles. There is more information about the effects of substrate stand-off distances in the condition of 10 micron particles.

The average impact velocity of 10 μm particles, as shown in *Tables 2.5*, at a substrate stand-off distance of 200 mm, is about 240 m/s and has an average landing location close to 11.5 mm away from the nozzle centerline. The velocity of the same particles at a distance of 250 mm is slightly higher in the order of 260 m/s. This is due to the fact that the strength of the bow shock formed at this distance is lesser than the one formed at 200 mm. This effect can also be understood by looking at the average landing location of these particles. The average landing location of the 10 μm particles at 200 mm is slightly more than the landing location at 250mm. On further increasing the stand-off distance to 300 mm, the impact velocity is found to be decreased. The impact velocity at this distance is around 230 m/s, which is lower than the one at 250 mm and 200 mm. The average landing location is around 11.5 mm, which is slightly above the landing location of the other two cases. Even though the strength of the bow shock formed at distance of 300 mm from nozzle exit would be low when compared to the bow shock formed at a closer distance, the particles have to travel through a long distance. This is the reason for reduction of impact velocity of particles in this distance. At this stage it can be expected that any further increase in the substrate stand-off distance would result in lower particle impact velocity and more deviation from the centerline. From *Table 2.5* the impact velocity at 350 mm from the nozzle exit is around 200 m/s and the average landing

location is around 12.6 mm. Although the strength of the bow shock formed at this distance would be very low, the 10 μm particles lose much momentum as they travel through a relatively large distance (of 350 mm) resulting in a low impact velocity.

It is quite interesting to see the characteristics of the 30 micron particles over the change in substrate stand-off distance. The impact velocity of these particles on a substrate at 200 mm from the nozzle exit is around 610 m/s with an average landing location very close to 3 mm from the centerline. As the stand-off distance is increased further, the impact velocity decreases constantly so that the impact velocity at 350 mm is around 480 m/s. This shows that these particles are least affected by the bow shock present near the substrate, but they decelerate as they travel through the distance. This is due to the fact that 30 μm particles show a poor response to the changes in the gas phase characteristics because of the relatively large Stokes number associated with them. This can also be understood by observing the average landing location; there is very little change in the average landing location when the stand-off distance is increased.

The characteristics of the 60 micron particles show a similar trend as that of the 30 micron particles. The average impact velocity of these particles at a distance of 200 mm is around 640 m/s which is also very close to that of the 30 micron particles at the same stand-off distance. Increasing the substrate stand-off distance yields, a reduction in their average velocity but, this rate of reduction is very low when compared to 30 micron particles. This is again due to the very large Stokes number associated with these particles, and therefore they are completely reluctant to the changes in the gas phase

characteristics. This can further be understood by observing the trend of the average landing location which is very similar to that of the 30 μm particles. Any further increase in the particle size shows a very similar trend in terms of both landing location and impact velocity. It should also be mentioned that a large particle size would result in a very poor coating quality, which is undesirable in any thermal spray process.

The above analysis can be summarized as follows. The characteristics of the 1 μm particles are severely affected by both the shock diamonds and the bow shock irrespective of the substrate stand-off distance. Increasing the particle size to 10 μm demonstrates a clear trend in particle characteristics with respect to the change in stand-off distances. The impact velocity of these particles at 200 mm is slightly lower than the one at 250 mm due to the comparatively strong bow shock formed on the substrate kept at 200 mm. Any further increase in the stand-off distance shows a reduction in the impact velocity and a reduction in the strength of the bow shock. This is because of their small size and low Stokes number. This shows that these particles respond sharply to the changes in the gas phase. The trend of the 30 μm particles and 60 μm particles are very similar to each other that they show a very poor response to either shock diamonds or bow shock due to their large Stokes number.

The results revealed by the above analysis demonstrate that the substrate stand-off distance plays an important role in improving the chances of particle landing on the substrate. If the particle size is lower than 30 μm, then it is appropriate to place the substrate at 250 mm as placing the substrate too close would result in stronger bow shock

formation and placing it too far might decrease the chances of obtaining large particle impact velocity which is required for a good coating quality. If the particle size is greater than 30 μm, a closer stand-off distance can be used but a low substrate stand-off distance might result in over-heating of the substrate.

Postulating a precise value for the ideal substrate stand-off distance is not possible as many other factors are also involved in this such as the effects of particle loading, which is discussed in detail in Chapter 3. The above analysis however, shows the complexity of the relation between particle size and the substrate stand-off distance.

2.3.5. The Effects of Substrate Configuration

The effects of substrate geometry on the trajectory of particles are discussed in this section. In order to study the effects of substrate geometry, three different configurations were studied; flat, concave and convex. *Figure 2.12* shows the Mach number line contour of gas flow in a free jet, gas flow impinging on a flat, concave and convex substrate. From the figure it is evident that there exists a significant difference in the flow Mach number in the regions near the substrate. The strength and pattern of bow shock seems to vary with respect to the substrate configuration and this will also influence the trajectory as well as the velocity of particles in its vicinity.

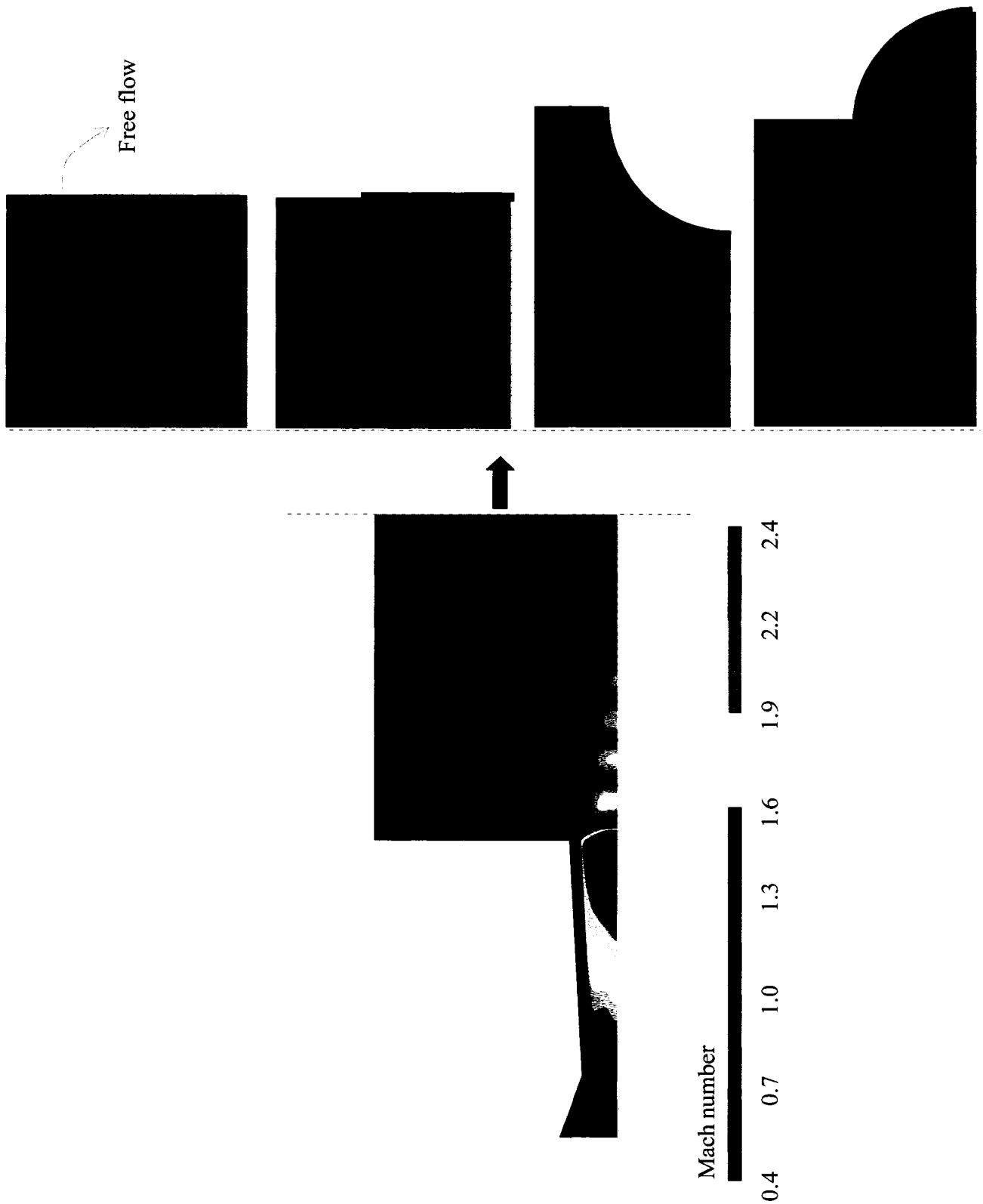

Figure 2.12: Gas phase Mach number contour for a (a) without substrate (free jet), (b) flat (c) convex and (d) concave substrates

The effects of substrate configuration and hence the effects of bow shocks on the particle trajectories are studied and the results are presented in *Figures 2.13 and 2.14*. Particle sizes considered for this study are 10 and 30 μm. These two sizes are considered because they represent the general trend of the particles with sizes from 1 μm to 60 μm. In order to clearly visualize the particle trajectories only 10 particle streams are presented in *Figure 2.13* and *Figure 2.14*.The trajectories of these particles impinging on flat, convex and concave substrates are studied. The flat substrate extends 25 mm in length from the nozzle central axis, while both the concave and convex substrates have a radius of curvature as 25 mm. All the substrates are located at a distance of 250 mm from the nozzle exit. Particle characteristics at a distance of 250 mm in a moving jet are compared with particle characteristics impinging on different substrates.

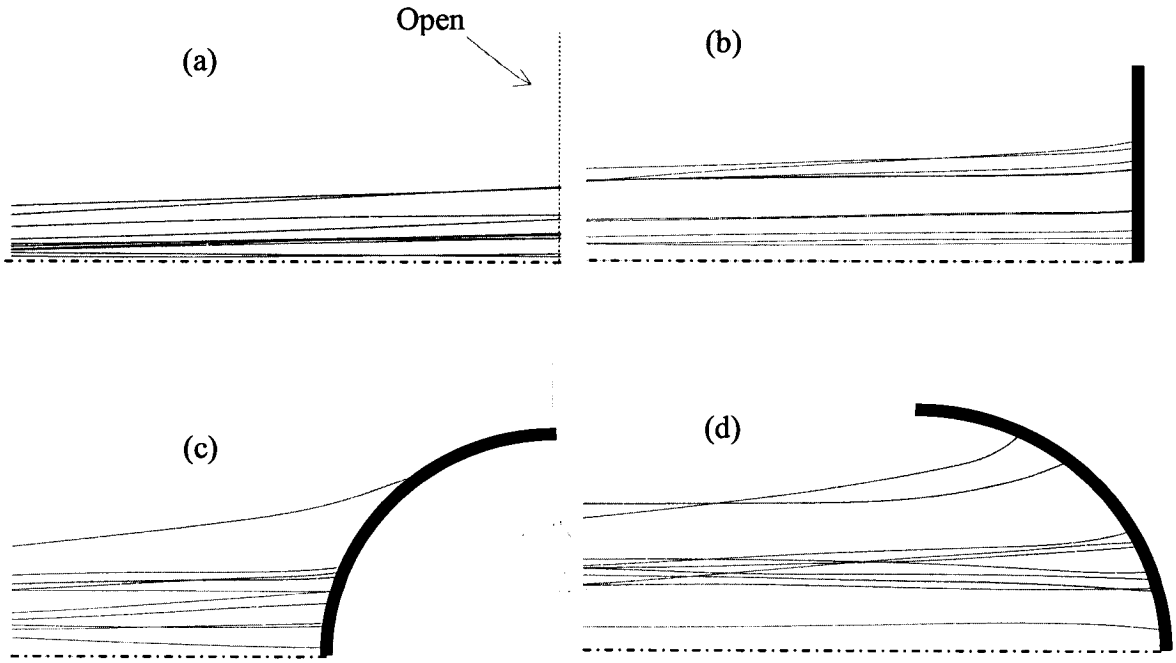

Figure 2.13: Trajectories of 10 μm particles in a (a) free jet, (b) flat substrate, (c) convex substrate and (d) concave substrate

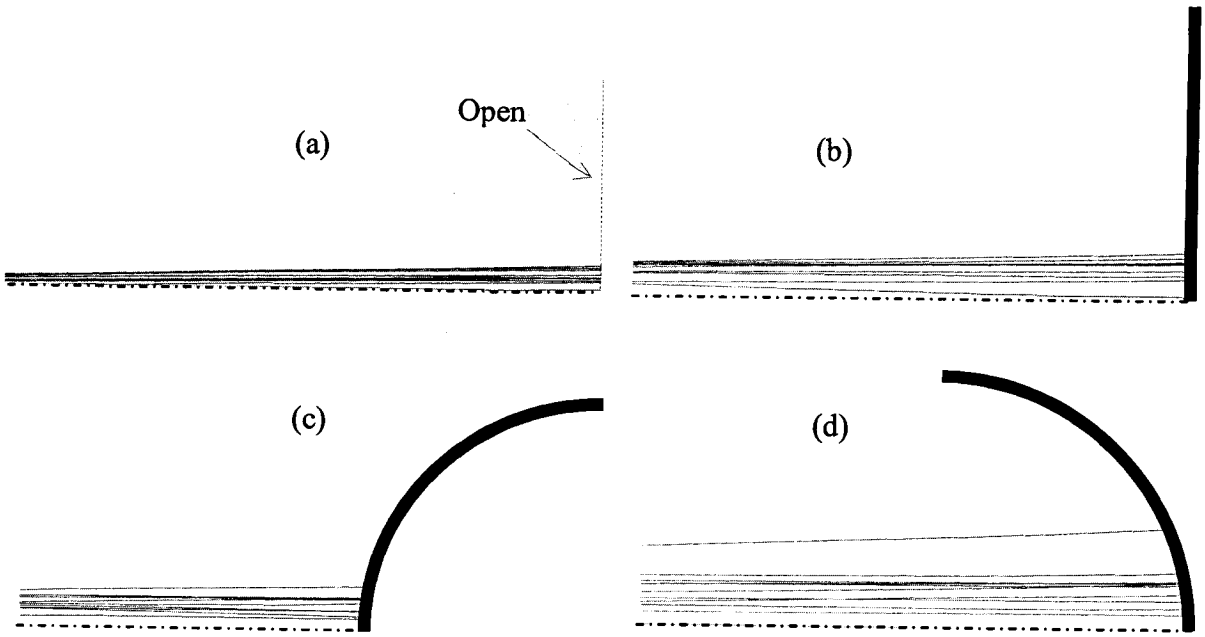

Figure 2.14: Trajectories of 30 μm particles in a (a) free jet, (b) flat substrate, (c) convex substrate and (d) concave substrate

By comparing *Figure 2.13a* and *Figure 2.13b*, it is obvious that the presence of a substrate in the flow field affects the flow of 10 μm particles. This change can also be seen on particle trajectories near a convex substrate and concave substrate. It is very interesting to see from *Figure 2.13d* that trajectories near a concave substrate are more scattered than those trajectories near a convex substrate. Though a concave substrate has a favorable shape to capture the particles, as shown in *Figure 2.12*, bow shock formed on such a shape are stronger than the ones formed on a flat substrate or a convex substrate. This effect will be more pronounced on smaller particles especially at lower stand-off distances.

Figure 2.14 shows the particle trajectories of 30 μm particles near different substrate configurations. It is very clear from the figure that the trajectories are almost same in all the cases except with some minor differences in the case of particles near the concave substrate, which is due to the high strength of the bow shock that is formed in this case. The absence of significant changes in these particle trajectories in the vicinity of bow shocks can be attributed to the large Stokes number associated with them.

In order to clearly understand the effects of substrate configuration, it is essential to study particle characteristics near each substrate. Characteristics for 10 μm and 30 μm particles are studied by plotting the impact velocity against the average particle landing on the substrate. For a flat substrate, the axial velocity of the particles is the impact velocity, whereas for particles impinging on a concave or convex substrate, it is the normal velocity, which is the impact velocity. The normal impact velocity is calculated as suggested by *Zhu et al.* [10].

Figures 2.15 shows the particle characteristics of 10 and 30 μm particles moving in a free jet. The shaded area under the dotted line is the area covered by the substrate, which implies that any particle that is present out of this shaded region, does not land on the substrate. *Figure 2.15a* shows particle condition of the 10 μm at a stand-off distance of 250 mm, the respective values of mean velocity and average radial location along with their respective standard deviation is tabulated in *Table 2.5*.

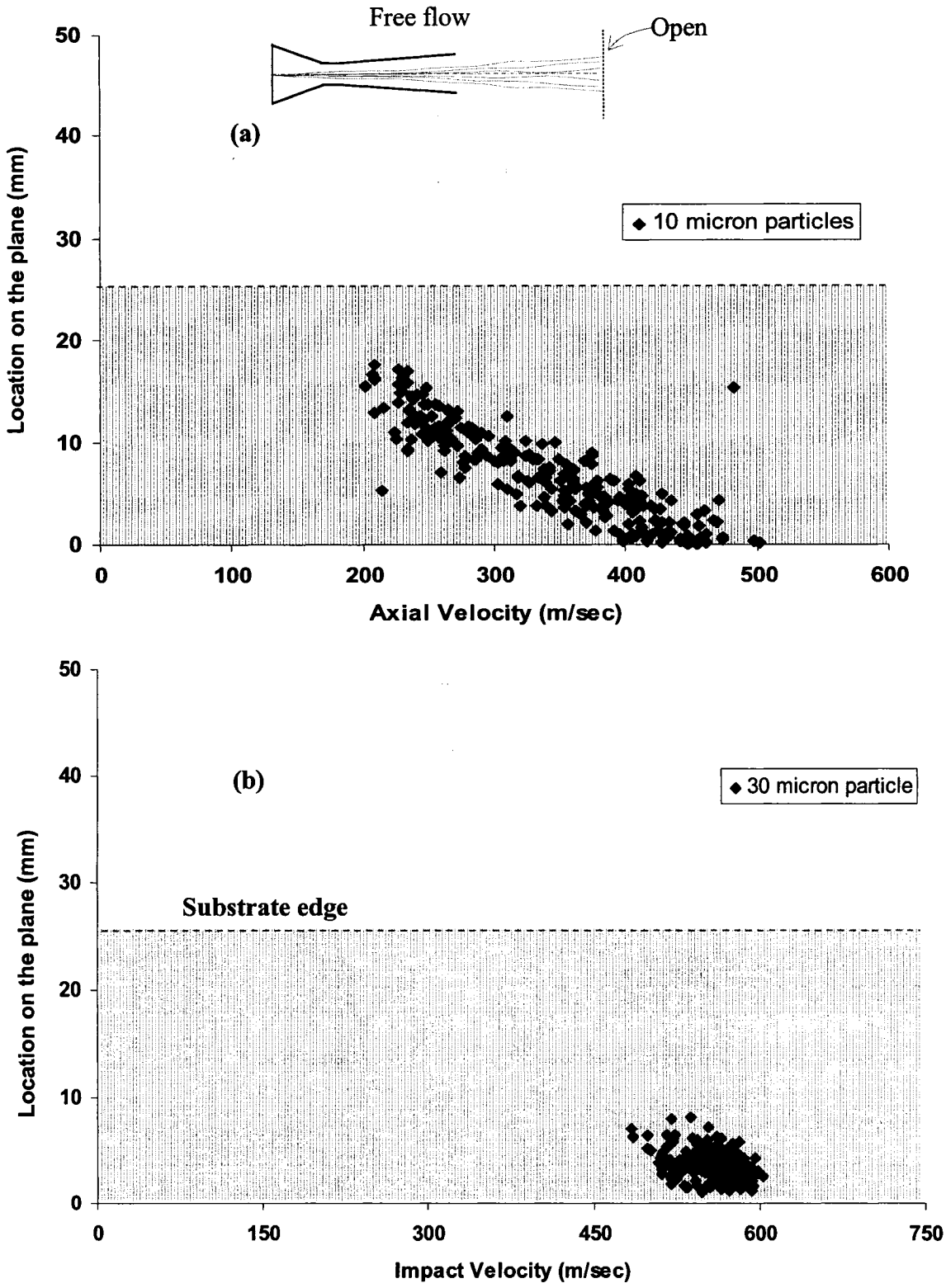

Figure 2.15: Particle conditions of size (a) 10 μm and (b) 30 μm flowing in a free jet

Table 2.6: Particle conditions moving in a free jet

Particle Sizes (μm)	Average Velocity (m/s)	Std. dev. (m/s)	Mean radial location (mm)	Std. dev. (mm)
10	336	42.52	6.21	2.34
30	570	12.33	3.17	1.51

It is evident from the figure and the table that the mean velocity of 10 μm particles at 250 mm from nozzle exit is 336 m/s with a standard deviation of 42.5 m/s, while the average radial location around 6 mm with standard deviation close to 2.5 mm. The mean axial velocity of the 30 μm particles are slightly less than 600 m/s with a standard deviation equal to 12.33 m/s. Because of the relatively large size associated with 30 μm particles average radial location is about 3.2 mm with very small standard deviation of 1.51 mm. This observation demonstrates the particle behaviour flowing in a flow in the absence of a substrate.

The trajectories of the 10 μm particles are affected by the series of shock diamonds that are present at the nozzle exit as a result of which, they lose momentum and hence are decelerated, whereas the 30 μm particles due to the large Stokes number are not affected by the presence of shock diamonds thus travel with sufficiently large velocity even at a distance of 250 mm from the nozzle exit.

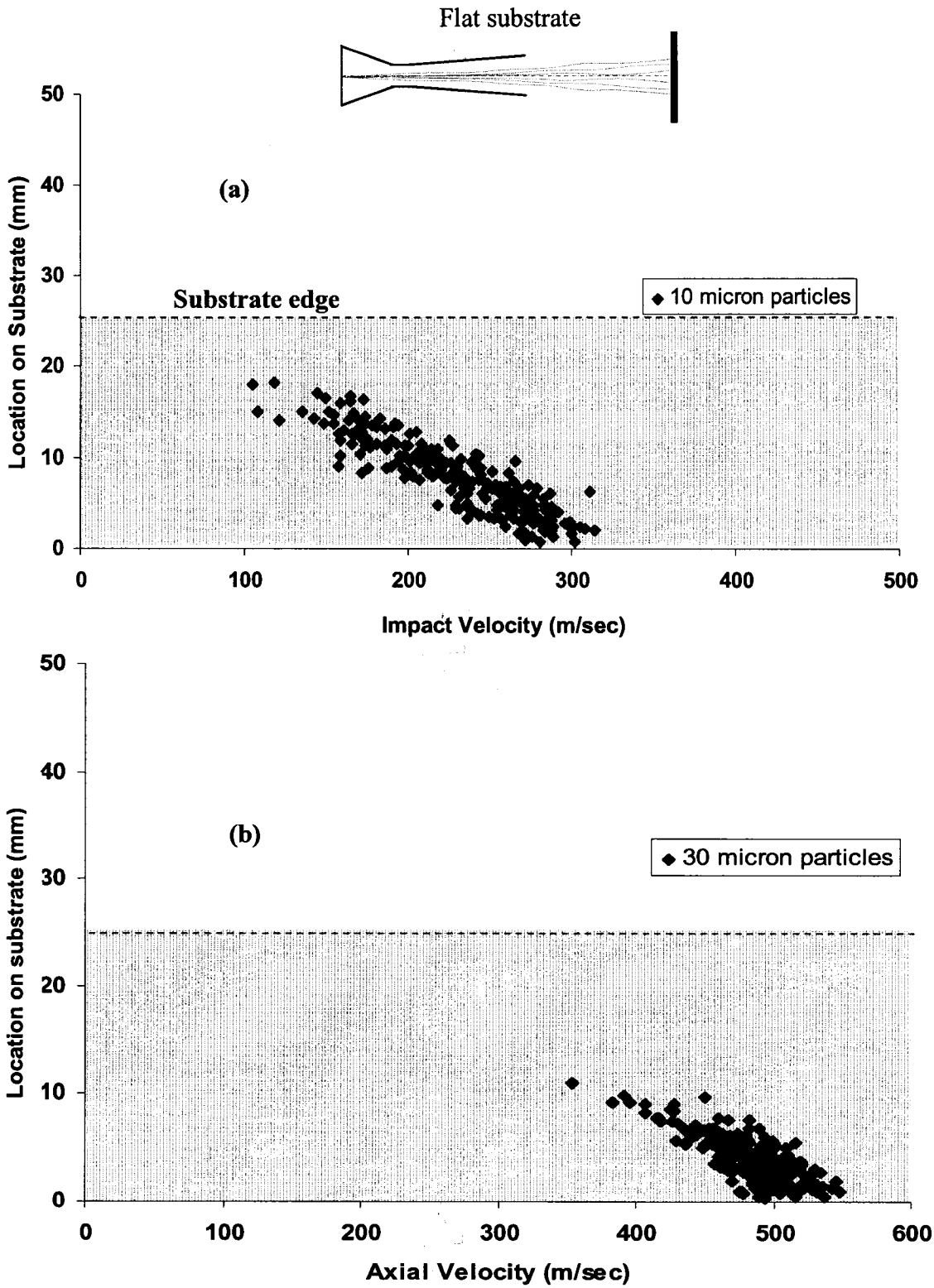

Figure 2.16: Particle conditions of size (a) 10 μm and (b) 30 μm impinging on a flat substrate

Figure 2.16 shows the characteristics of those particles impinging on a flat substrate, while *Table 2.6* tabulates the respective values. It can be seen that the average impact velocity is close to 260 m/s against 350 m/s, which is the velocity of the same type of particles flowing in a free jet at the same stand-off distance. The respective standard deviation has increased from 42 m/s to 53 m/s. The average landing location of these particles is about 10.2 mm with a standard deviation of 6 mm off the nozzle centerline. This is due to the strong bow shock formed on the flat substrate which decelerates the particles abruptly in addition to shifting their mean lading location. When smaller particles leave the nozzle exit, they are severely affected by the shock diamonds which result in a considerable amount of momentum loss. When these particles arrive at the substrate they are further decelerated by the bow shocks which decrease the kinetic energy of particles. Such particles with low kinetic energy may not have enough momentum to penetrate the bow shock and hence these particles may not land on the substrate and even if they hit the substrate, they may not stick with the substrate, which results in poor coating quality.

While there is a considerable change in the characteristics of the 10 μm particles due to the bow shock, the 30 μm particles show a pattern similar to that of the one flowing in a

Table 2.7: Particle conditions impinging on a flat substrate

Particle sizes (μm)	Average impact velocity (m/s)	Std dev (m/s)	Mean location on substrate (mm)	Std dev (mm)
10	254	52.98	10.15	6.37
30	520	21.13	3.62	1.95

free jet. From *Table 2.6*, the average impact velocity of the 30 μm particles is equal to 550 m/s, which is very close to those in a free jet. The average landing location from the centerline is around 3.5 mm, which clearly shows that these particles are neither decelerated nor deviated from their path due to the presence of the bow shock or stagnation flow. The spatial and velocity distribution of these particles are very similar to those of a free jet case, which can be seen by comparing *Figure 2.16* and *2.17*. Therefore the presence of a substrate in the flow field does not have any effect on such particles.

Figures 2.17a and *2.17b* show characteristics of the particles impinging on a convex substrate, while *Table 2.7* tabulates the mean values of normal velocity of impact and landing location. It is obvious from *Table 2.7* that the mean particle normal velocity of impact on a convex substrate is around 280 m/s with a standard deviation of mean equal to 44 m/s. The average particle landing location is around 9 mm from the centerline with a standard deviation close to 5 mm. These results can be compared those of the case with flat substrate (see *Table 2.6*). It can be seen that the impact velocity near a convex substrate is more than the impact velocity impinging on a flat substrate. Also, the average landing location of particles is lesser than that of one near a flat substrate.

Table 2.8: Particle conditions impinging on a convex substrate

Particle sizes (μm)	**Average impact velocity (m/s)**	**Std dev (m/s)**	**Mean location on substrate (mm)**	**Std dev (mm)**
10	282	44.20	8.90	5.28
30	534	21.42	3.52	1.83

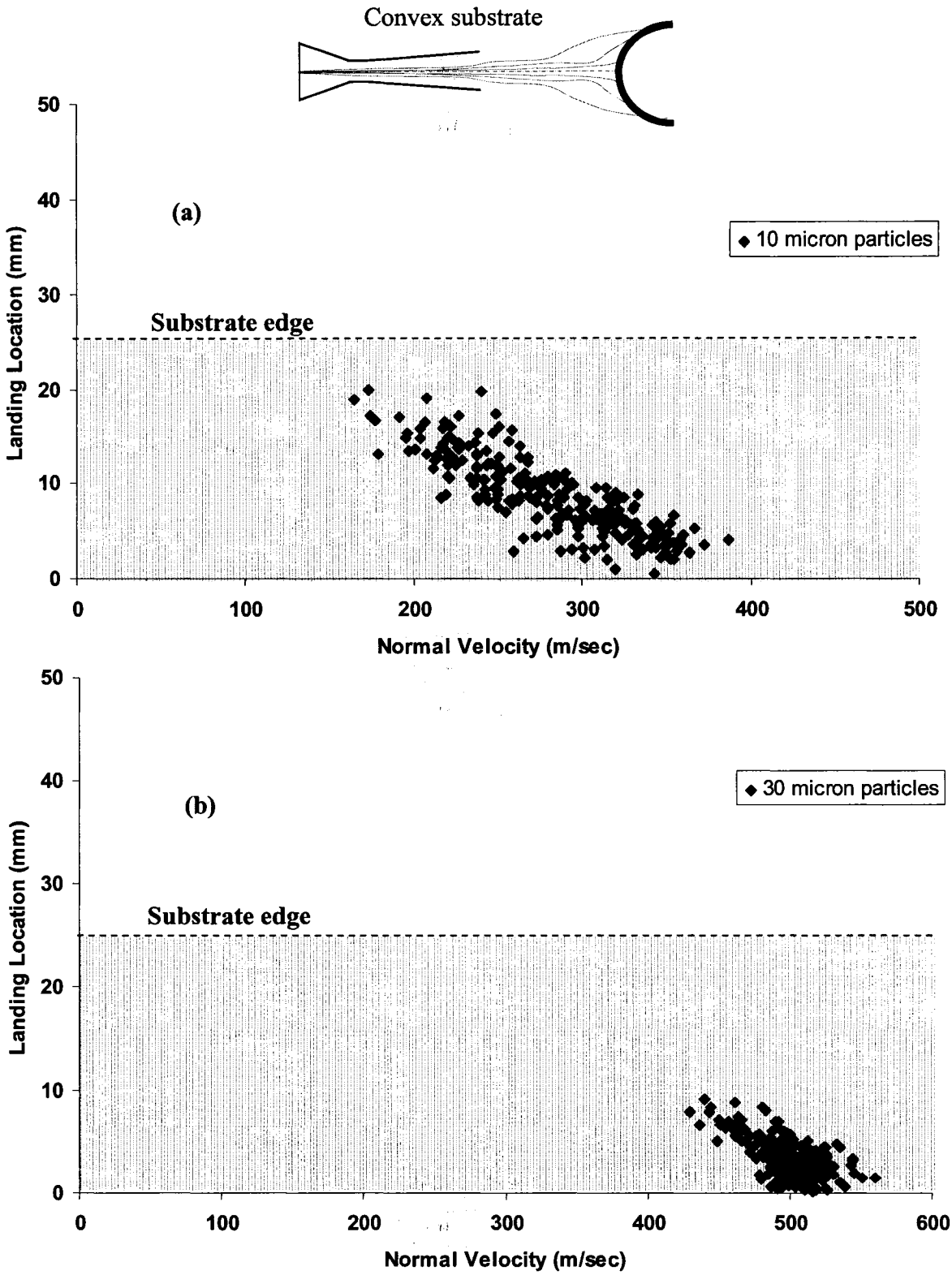

Figure 2.17: Particle conditions of size (a) 10 μm and (b) 30 μm impinging on a convex substrate

This implies that the strength of the bow shock formed on a flat substrate is stronger than one formed on a convex substrate. The characteristics of the 30 μm particles show a similar trend as with the flat substrate case, which are shown in *Figure 2.17*. From the *Table 2.7*, their average normal impact velocity is approximately 535 m/s and has an average deviation of 4 mm from the nozzle centerline. The respective standard deviations are 52.98 m/s and 5.48 mm. Both the impact velocity and landing location of the 30 μm particles near a convex substrate is very close to those particles of the same size impinging on a flat substrate, even though the particle velocity near a convex substrate is slightly higher compared to the velocity near flat substrate. This observation affirms that the bow shock formed on a flat substrate is stronger than the one formed on a convex substrate.

Figures 2.18a and 2.18b show the characteristics of the particles landing on a concave substrate. The corresponding values of mean velocity and particle landing location are presented in *Table 2.8*. It is evident that the average normal impact velocity reduces to as low as 150 m/s with large standard deviation close to 70 m/s. The average landing location is more than 12 mm, which is very high when compared to the particle characteristics of the other two cases. The standard deviation of mean landing location is in the order of 7 mm, which is large comparing to particles impinging on a flat or a convex substrate. The reduction in the impact velocity and increase in the average landing location is attributed to the very strong bow shock formed on this substrate. By comparing the condition of 10 μm particles through *Tables 2.6, 2.7* and *2.8*, it can be inferred that the bow shock formed on a concave substrate is much stronger than one

formed on a flat or convex substrate. *Figure 2.18a* shows that few particles fall outside the shaded region, which implies that these particles do not land on the substrate. In addition to this, many particles fall very close to the dotted line (edge of the substrate) with velocities less than 70 m/s. These particles have very low probability of landing on the substrate and even if they happen to reach the substrate they might not stick properly on the surface of substrate which will considerably reduce the deposition efficiency.

Figure 2.18b and *Table 2.9* shows the characteristics of the 30 μm particles impinging on a concave substrate. It can be seen that, the average impact velocity of these particles is around 470 m/s, which is much smaller than average velocities of same kind of particles impinging on either convex or flat substrate; the standard deviation is maximum among the three different configurations under study, namely 71 m/s Here the strength of the bow shock is clearly illustrated that even particles with large Stokes number (30 μm particles) are decelerated near the substrate. This effect can be further understood by observing the average landing location of these particles; it is around 4.1 mm with a standard deviation 2.12 mm, the maximum deviation among the three different configurations under study.

Table 2.9: Particle conditions impinging on a concave substrate

Particle sizes (μm)	**Average impact velocity (m/s)**	**Std dev (m/s)**	**Mean location on substrate (mm)**	**Std dev (mm)**
10	148	70.83	13.12	6.75
30	468	29.43	4.13	2.12

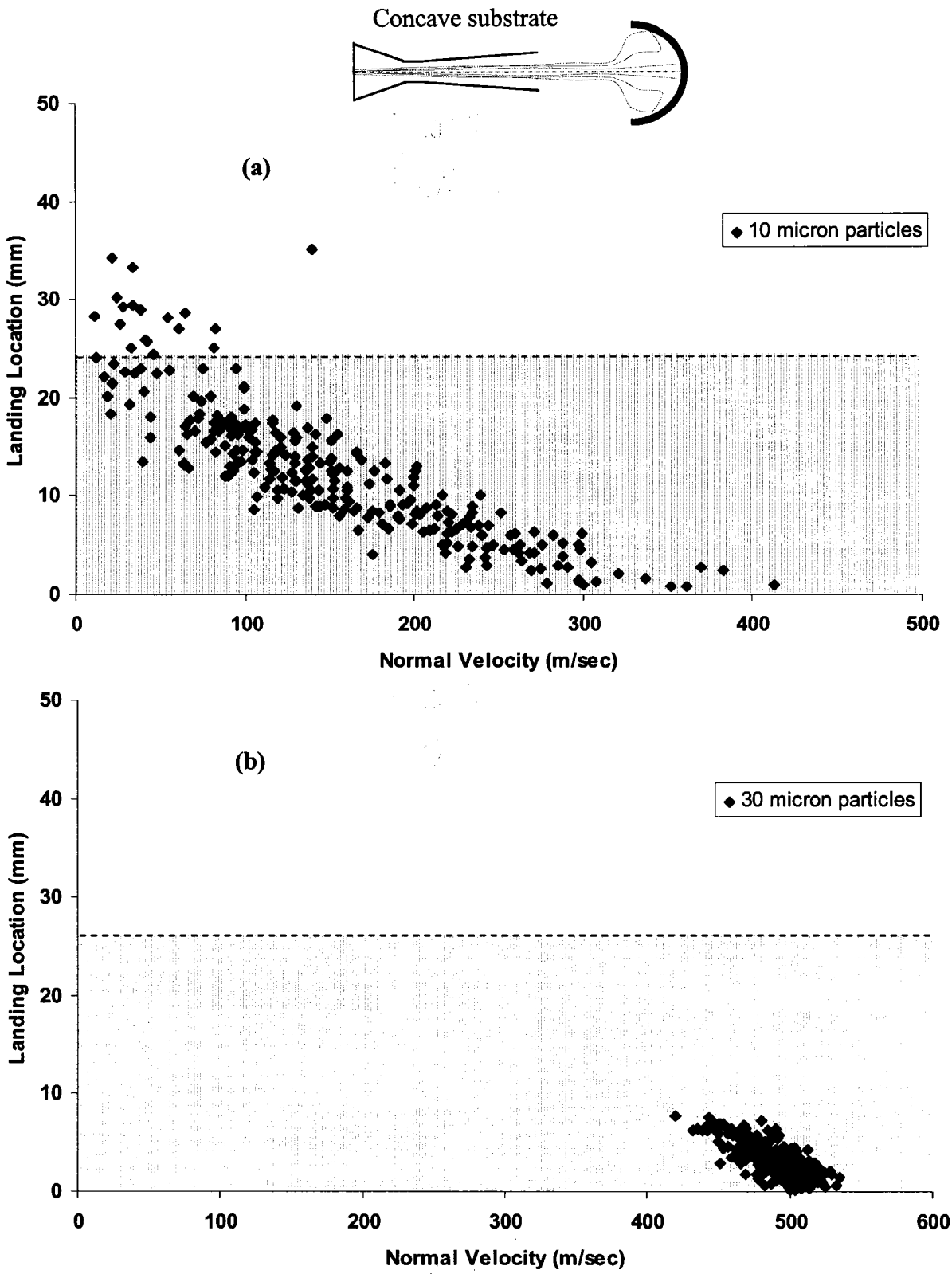

Figure 2.18: Particle conditions of size (a) 10 μm and (b) 30 μm impinging on a concave substrate

From the above analysis, it can be seen that flow impingement on substrates with different configurations gives rise to different flow patterns near the substrate with varying bow shock strength. It can also be understood that the bow shock formed on a concave substrate is much stronger than the one formed on either convex or flat substrate. It was observed that small particles with sizes 10 μm or less may not be able to penetrate the strong bow shock that forms due to the flow impingement on a concave substrate. Even heavy particles i.e. 30 μm showed notable response to the bow shock, as against the languid behaviour of these particles to the changes in the gas flow. This is an interesting observation revealed by numerical investigation of this phenomenon. It was expected that a concave substrate would capture almost all the particles fed due to its favorable curvature and incidentally many particles would escape near the convex substrate. On the contrary, it was observed that in terms of capturing smaller particles, the convex substrate is better than a flat substrate which in turn is better than a concave substrate.

This chapter was dedicated to studying changes in particle characteristics due to various changes in the gas phase i.e. shock diamonds and bow shock using the Lagrangian trajectory model. When the two-phase flow is dense, the particle injection and particle feed rate have severe impacts on the gas phase, which will be studied in Chapter 3.

3. Eulerian Approach

The intention of this chapter, as stated in the objective section *(see Section 1.7 and 1.8)* is to model the two-way coupling in a dense two-phase flow that occurs in an HVOF process and find out the effect of a dense particulate phase on the gas phase. By comparing the gas phase characteristics of a single phase flow with that of a two-phase flow with different particle loadings, a proper insight about the effect of particle volume fraction on the gas phase can be obtained. In order to obtain this, a fully Eulerian approach is used to model the two-phase dense flow and the results are discussed.

The Eulerian approach to a multi-phase flow problem implies the continuum assumption for both the continuous and dispersed phases This chapter provides a complete description of Eulerian approach, governing equations, and numerical techniques used to solve the HVOF problem by using 'Implicit Continuous-fluid Eulerian' (ICE) technique [38], [39] and [40]. The ICE method is a compressible finite volume numerical technique with all principle variables located at the cell center. The state variables are the total mass of species, momentum and energy. The phases are coupled by introducing the volume fraction term in the governing equations. Since mass, momentum and energy are conserved and there is no need to resolve shocks waves using the finite volume method.

The physical domain is divided into a number of arbitrary quadrilateral control volumes. A fully cell-centered state vector is employed. Therefore, all the dependent variables and fluid properties are stored at the control volume center (collocated or cell-centered arrangement). The data structure arrives from a multi-block, structured grid arrangement. The governing equations are solved over each control volume resulting in a system of non-linear algebraic equations which are solved simultaneously.

3.1. Governing Equations

The governing equations are continuity, momentum and energy equations for compressible, non-reactive multi-material flow at continuum level [38],

$$\frac{\partial \rho_k}{\partial t} + \nabla \rho_k \vec{U}_k = 0 \tag{3-1}$$

$$\frac{\partial \rho_k \vec{U}_k}{\partial t} + \nabla \rho_k \vec{U}_k \vec{U}_k = -\theta_k \nabla p - \nabla \theta_k \left(p^o{}_k - p\right) - \nabla \bullet \left(\alpha_k \rho_o \vec{U'}_k \vec{U'}_k\right) + \nabla \bullet \left(\alpha_k \tau_o\right) + \rho_k \vec{g} + \Sigma \theta_k \theta_l K_{k,l} \left(\vec{U'}_l - \vec{U'}_k\right) \tag{3-2}$$

$$\frac{\partial \rho_k e_k}{\partial t} + \nabla \rho_k e_k \vec{U}_k = -p_k \nabla \cdot \vec{U}^f + \alpha_k \gamma_o^{-1} \left(p^o{}_k - p\right) - \nabla \bullet \left(\alpha_k \rho_o e_o \vec{U'}_k\right) + \frac{\alpha_k \tau_o : \varepsilon}{2} - \nabla \cdot \alpha_k q_k + \Sigma \theta_k \theta_l R_{k,l} \left(T_l - T_k\right) \tag{3-3}$$

where $\vec{U'}$, ρ, p, e, T, τ_o, K, *and* R represents the velocity vector, density, pressure, internal energy, temperature, stress tensor, momentum and heat exchange coefficients between the phases, respectively; α is the volume fraction and θ being the expected

value of volume fraction. The subscript l and k refers to the fluid and solid material, respectively. As the flow under study is non-reactive the conversion of material into a product is absent and hence the continuity is equal to zero. The non-equilibrium condition results in an equation for θ_k and is expressed as follows:

$$\frac{\partial \theta_k}{\partial t} + \nabla \cdot \theta_k \vec{U}_k + \nabla \cdot \left(\alpha_k \vec{U'}_k \right) = 0 \qquad (3\text{-}4)$$

This equation is constrained by the fact that for both equilibrium and non-equilibrium state, $1 - \sum_m \theta_m = 0$ is always true. The turbulence is modeled by using the two-phase k-ε turbulence model of Kashiwa [38].

For a compressible flow, there is one continuity equation, three momentum equations, and an energy equation that need to be solved. But the above mentioned equations have seven unknowns namely ρ, p, e, T, u, v and w. This makes the system incomplete and a need arise to introduce two more equations. The two additional equations used to close the system of equations are obtained by determining relations between the thermodynamic variables. For constant specific heats the equation of states can be given as follows:

$$p = (\gamma - 1)\rho e \qquad \text{and} \qquad T = \frac{(\gamma - 1)}{R} e \qquad (3\text{-}5)$$

where, γ is the specific heat of the ideal gas. The momentum is exchanged between the two phases by the movement of particles with a relative velocity to the gas flow. The force acting on a single sphere, moving with a velocity of U_{rel} is given by

$$F_D = \frac{1}{2}\rho_g U_{rel}^2 C_D A \tag{3-6}$$

where ρ_g, U_{rel}, C_D and A are density of the gas phase, relative velocity between the gas and particle, drag coefficient, and area of the particle, respectively. When there are N particles (of equal area) in the flow field, then the volume fraction of the particulate phase becomes as follows:

$$\theta_p = \frac{4}{3}\pi r^3 N \tag{3-7}$$

where θ_p is the particulate phase volume fraction. Hence, the force acting on the particle phase per unit volume is:

$$\vec{F}_D = \rho_c \left|\vec{U}_{rel}\right| \vec{U}_{rel} C_D \theta_p (3/4r) \tag{3-8}$$

where, r is the radius of particles. This force for a multi-material form can be written as:

$$\vec{F}_{l,k} = \sum_l \theta_k \theta_l K_{k,l} \left(\vec{U}_l - \vec{U}_k\right) \tag{3-9}$$

where, K is the momentum exchange coefficient. For a two-phase gas particle flow the momentum exchange coefficient is as follows:

$$K_{l-k} = K_{k-l} = \left(\frac{3}{8}\right) C_D \frac{\rho_c}{\theta_c} \frac{\left|\vec{U}_{rel}\right|}{r} \tag{3-10}$$

Similar to the momentum transfer between the phases, heat is also transferred and the heat exchange coefficient is represented as follows:

$$R_{k-l} = R_{l-k} = \frac{\rho_l}{\theta_l} h_c \frac{\left|\vec{U}_{rel}\right|}{r} \tag{3-11}$$

where, h_c is the convective heat transfer coefficient, per unit area. The following assumptions are made in the integration and discretization of the governing equations:

- The non-equilibrium pressure term and the multiphase Reynolds stress are assumed to be zero.
- The multi-phase fluctuational transport of energy, average viscous dissipation and thermal transport by conduction terms are assumed to be zero.
- The mesh velocity is zero and the mesh is structured.
- A first-order finite difference scheme is used for the time derivatives.

3.2. Numerical Technique

In this section, equations in the discretised form are presented for a single-phase compressible flow. *Figure 3.1* shows a typical grid arrangement. The following convention is used for indexing the mesh; *i, j,* and *k* are the indices used for x, y, and z direction, respectively. The faces of the cell are named as follows; L, R, B, T, BK, and FR represents left, right, bottom, top, back and front, respectively. For example the x-component of the face centered velocity across the front faces of the computational cell *i, j, k* can be given as $u^f_{i,j,k,F}$. In addition to this, for each of the computational domain there are two layers of ghost cells that surround the domain.

3.3. Algorithm Description

This part of the work uses CFDLib, a freely distributed set of source codes developed by Los Alamos National Laboratory. The governing equations are solved for time dependent case, where the steady state solution is found by marching through time until the variables do not show variation between successive time steps. The combustion of oxy-fuel is not modeled as the solver used for solving the problem does not have combustion modeling feature, explaining various reaction chemistry. Instead the results of the combustion are given as input to the problem. The computational cycle can be divided into three main steps namely:

- Calculation of the auxiliary quantities as a first step,
- A Lagrangian step, in which the effects of physical processes are computed, and
- An Eulerian step, in which the state is mapped to a common control volume.

This algorithm is called as Arbitrary Lagrangian Eulerian (ALE) technique. The advantages of using this technique is, its clear distinction of separating physical process and mesh interpolation, and its ability to use arbitrarily moving meshes [41].

As mentioned earlier, all the dependent variables and fluid properties are stored in the center of cell i.e., control volume; this is also called a 'collocated' or a 'cell-centered' arrangement. The basic algorithm used for solving quantities over time is given as follows. Superscripts c and f represent cell-centered and face-centered quantities, respectively. The computational cell arrangement is shown in *Figure 3.1.*

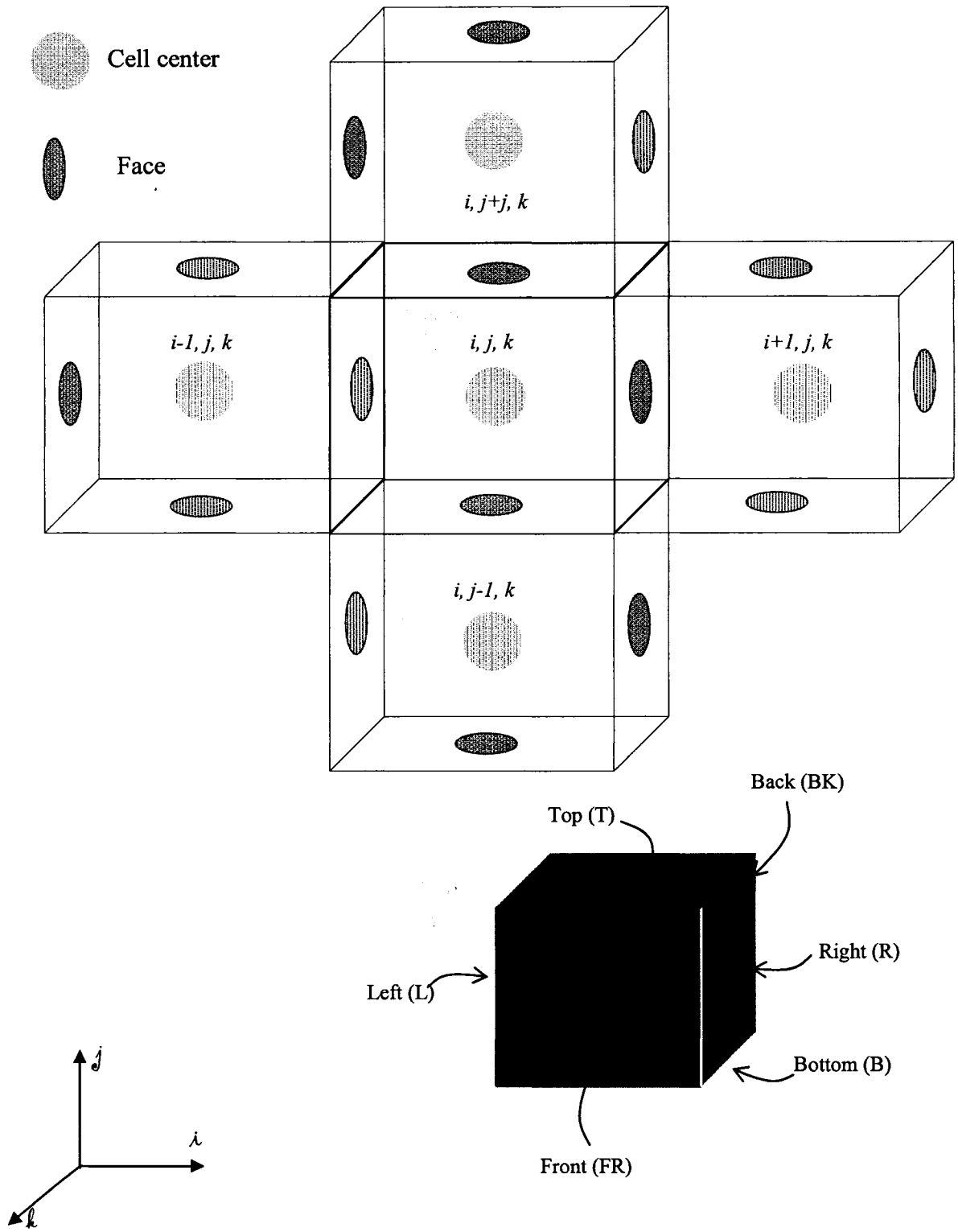

Figure 3.1: Grid arrangement and cell face labeling

Step 1:

Pressure, at the cell center is calculated from equation of state for an ideal gas stated in equation 3-12, in an explicit step.

$$p^{(n+1),c} = (\gamma - 1)\rho^{n,c} e^{n,c} \qquad (3\text{-}12)$$

Step 2:

The Lagrangian pressure at the $(n+1)^{th}$ cell center, $p_L^{(n+1),c}$, and a face centered velocity at the $(n+1)^{th}$ step, $\vec{U}^{(n+1),f}$, are calculated using a linear approximation to the pressure [42] . This is a semi-implicit finite difference step.

Step 3:

In step 3, the face-centered pressure, $p^{(n+1),f}$, is calculated explicitly using the continuity of acceleration principle.

Step 4:

Having calculated $\Delta p^{(n+1),c}$ and $p^{(n+1),f}$, from steps 2 and 3, sources terms of momentum and energy are calculated. For a single material case, this is an explicit step.

Step 5:

In this step, the Lagrangian values $m_L^{(n+1)}$, $\left(m\vec{U}\right)_L^{(n+1)}$ and $e_L^{(n+1)}$ are calculated, which are the sum of source term calculated in step 4.

Step 6:

The advection of mass, momentum and energy using the face centered fluxing velocities, $\vec{U}^{(n+1),f}$, from step 2 is calculated explicitly.

Step 7:

Mass momentum and energy quantities, which were calculated by the summation of Lagrangian values (from step 5), and advection term from step 6, are updated.

3.3.1. Computational Domain and Boundary Conditions

The computational domain is as shown in the *Figure 3.2*. The nozzle has three inlets for particle-carrier gas, pre-mixed oxy-fuel and coolant. The combustion is not modeled, however the results of combustion process modeled in Chapter 2 is given as inlet condition to the HVOF gun. Nitrogen is injected in all the ports at 350 K, while at the

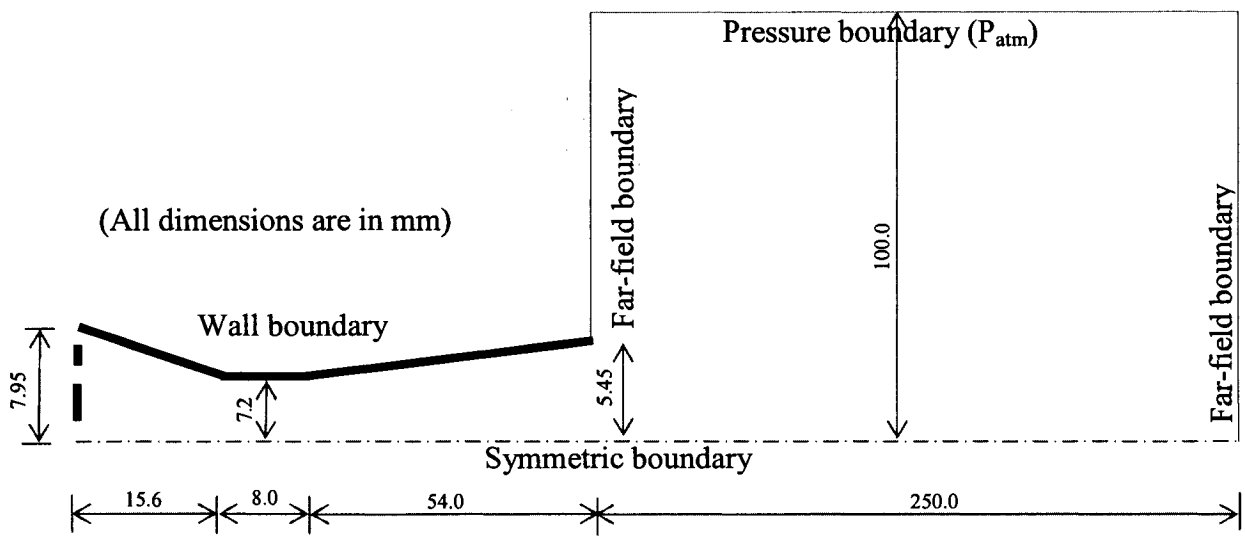

Figure 3.2: Computational Domain and boundary conditions

middle port at a temperature of 2800 K, to account for rise in temperature due to the combustion phenomenon. Particles with uniform size of 30 μm are injected through the central port along with carrier gas. Symmetric boundary condition is applied along the nozzle centerline. The computational domain extends up to 250 mm in the axial direction and 100 mm in the radial direction, outside the nozzle exit. No-slip wall boundary condition is applied at nozzle walls, while a far-field boundary is applied at the end of computational domain. In order to initiate the computations, an atmospheric pressure boundary is applied at the radial end of the domain.

3.3.2. Mesh and Discretization

The main concern in using the Eulerian approach for modeling a dense suspension flow is to ensure the continuity of the dispersed phase or particulate phase. The mesh size should be selected in such a way that the control volume contains sufficient number of particles in order to ensure the continuity assumption to be reasonable. The computational domain inside the nozzle contains 40 radial and 116 axial cells and the domain outside the nozzle consists of 250 cells in the axial direction and 100 cells in the radial direction.

3.4. Results and Discussion

The HVOF process is numerically simulated using the Eulerian two-fluid model and the results are discussed in this section. The results of single-phase (without particle injection) are first presented, and these results are compared with the results including particle injection. This way the effect of two-way coupling can be easily visualized.

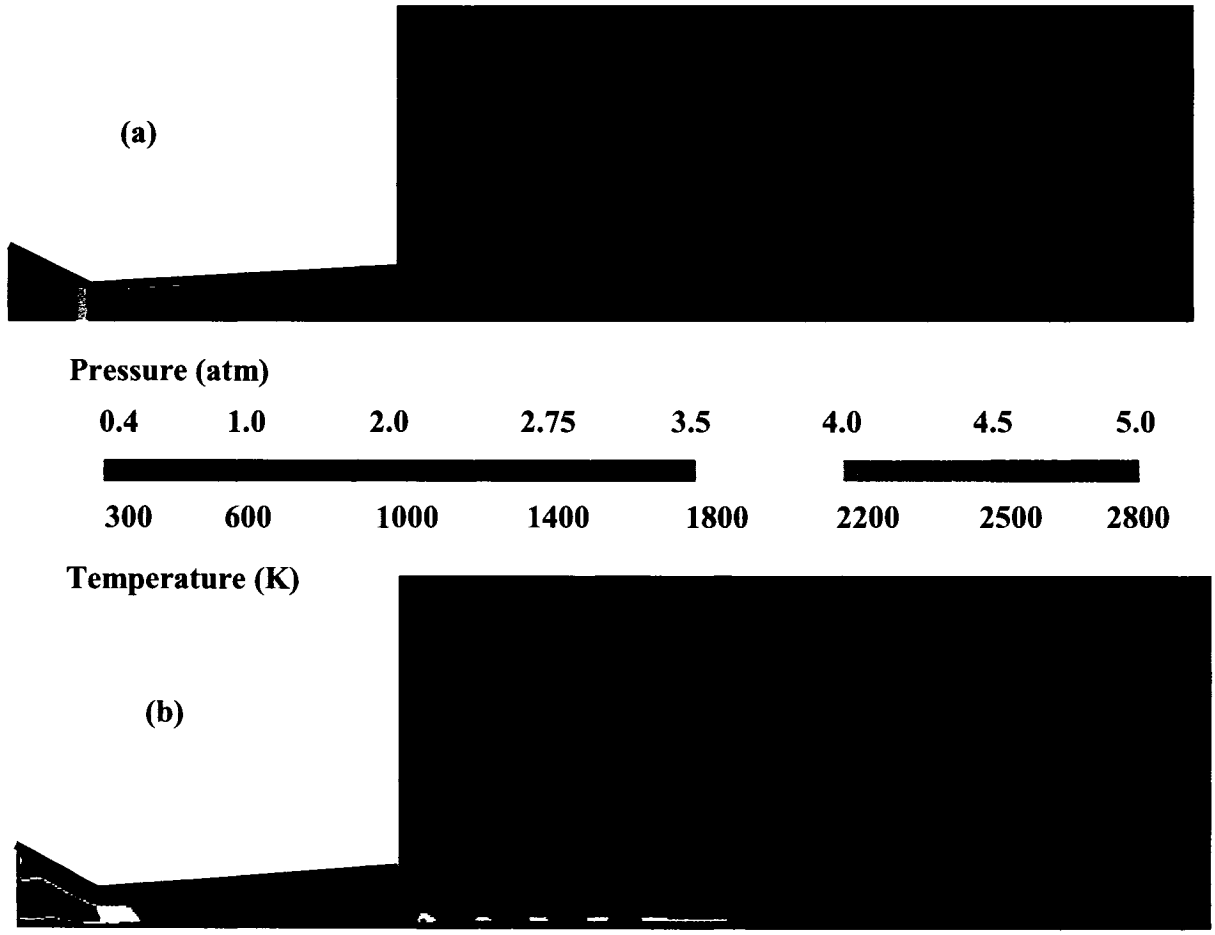

Figure 3.3: Gas phase contours of (a) Pressure and (b) Temperature

Figure 3.3 (a) and *(b)* show the gas phase contours of pressure and temperature, respectively. As explained earlier, the results of combustion are given as input, which raises the gas pressure above 5 atmospheres. The gas expands as it travels through the nozzle; it becomes over expanded when it reaches the nozzle exit. The flow adjustment to atmospheric pressure is attained by undergoing a series of expansion and compression waves, known as shock diamonds. From the *Figure 3.3 (a)*, it can be seen that there are 4 to 5 shock-diamonds occur before the flow finally adjusts to the atmospheric pressure.

Temperature variation across these shock waves can be clearly seen in *Figure 3.3 (b).* The temperature of the gas near the inlet is around 2700 K due to the combustion of fuels, whose results are given as input. The temperature of the gas, as it travels through the length of the nozzle, comes down to around 1600 K. At the nozzle exit, due to the presence of shocks, the gas temperature suddenly rises to 2500 K and thereafter the temperature of gas temperature fluctuates between 1500 K and 2500 K due to the alternatively expanding and compressing shock waves. After these shock diamonds, the temperature of the gas settles down to around 1600 K.

Figure 3.4 shows the velocity contour below which the centerline Mach number is plotted against the nozzle axial distance. It is evident from the figure that the velocity of the gas accelerates due to the high pressure at the nozzle inlet (as seen from *Figure 3.3*) and as the gas reaches the throat, the Mach number becomes 1, which can also be seen from the Mach number plot. The gas expands further in the divergent section of the nozzle and when it reaches the nozzle exit, the Mach number of the gas is about 2.4. The shock diamonds at the nozzle exit (which was explained in *Figure 3.3(a)*) can also be seen in the velocity contour. The velocity fluctuates between 700 m/s to 1500 m/s before it finally settles down to around 900 m/s, after which the flow starts decelerating. The fluctuation in the Mach number plot is attributed to these shock diamonds. The Mach number at the nozzle exit is slightly above 2.3 which after undergoing 5 to 6 expansion and compression, finally settles down close to 0.75 of the sound speed. Thus the results of the gas phase with out particle injection obtained by using the Eulerian model are very similar to that of the results obtained by Lagrangian model (presented in Chapter 2),

except that the shock diamonds captured using the Eulerian model are not as clear or as sharp as the results of the Lagrangian model. This can be attributed to the large mesh size of Eulerian model, which is essential for the continuum assumption of both the phases.

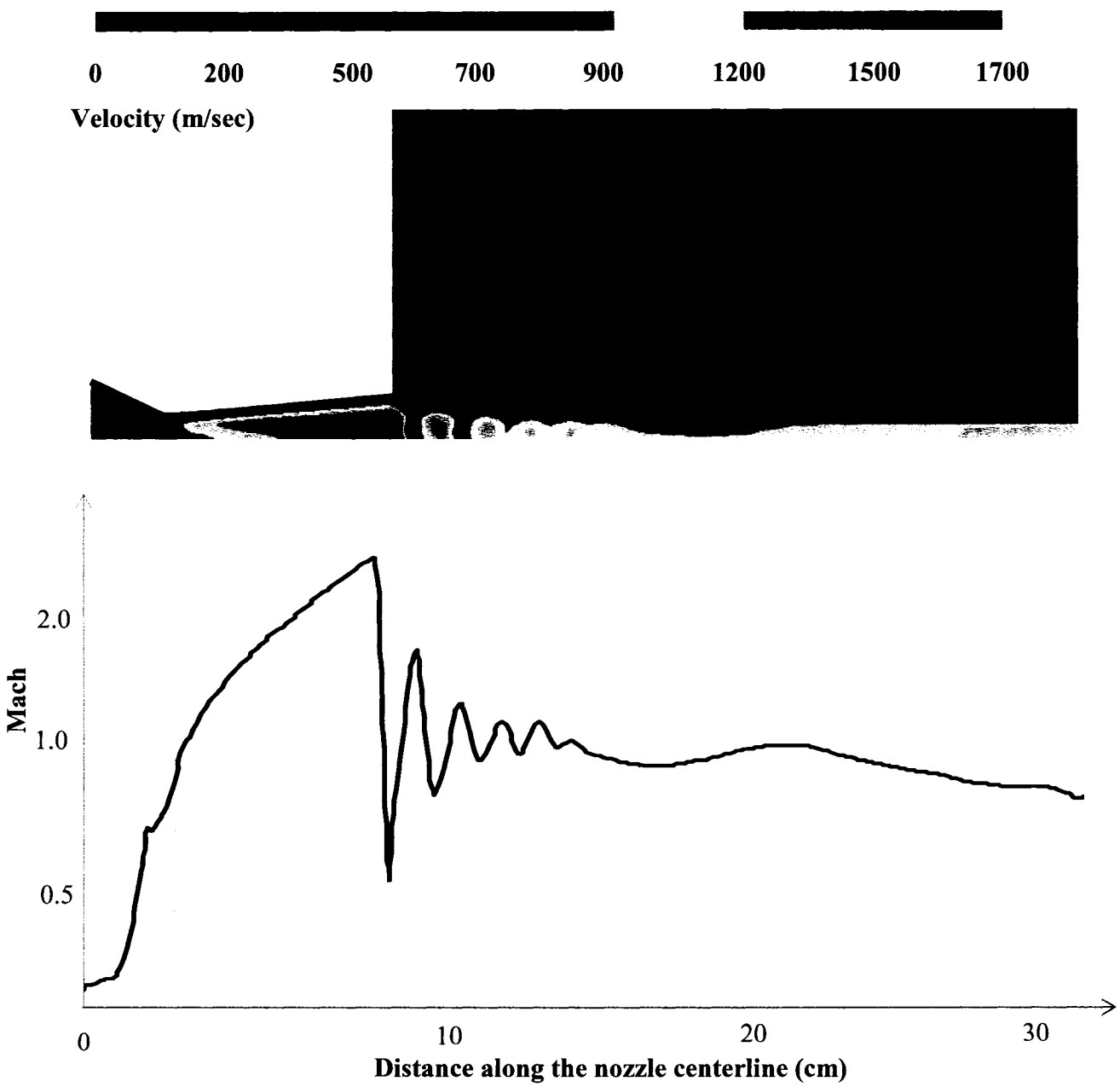

Figure 3.4: Gas phase velocity contour and plot of Mach number along the centerline

3.4.1. Effect of Particle Loading on Gas Phase

In a two-way coupled scenario, the effect of particle loading on the gas phase would be very significant depending upon the volume fraction of the particle phase; in a dense flow scenario the characteristics of the gas phase cannot be expected to be the same as in a single phase or dilute flow scenario. In a typical HVOF process, both types of flow scenario occur; dilute and dense. In the region near the nozzle centerline, the particle volume fraction would be higher, implying that the two-phase flow is dense. Nevertheless particle volume fraction would be almost zero in the regions far away from the centerline, meaning a dilute two-phase flow. This is very well evident from *Figure 3.5*. In the region where particle phase is dense, there would be a considerable change in the gas phase characteristic. To see the effect of particle injection (thereby effect of particle volume fraction) on the gas phase, it would be appropriate if the gas phase velocity contours are compared before and after particle injection, which is presented in *Figure 3.6*.

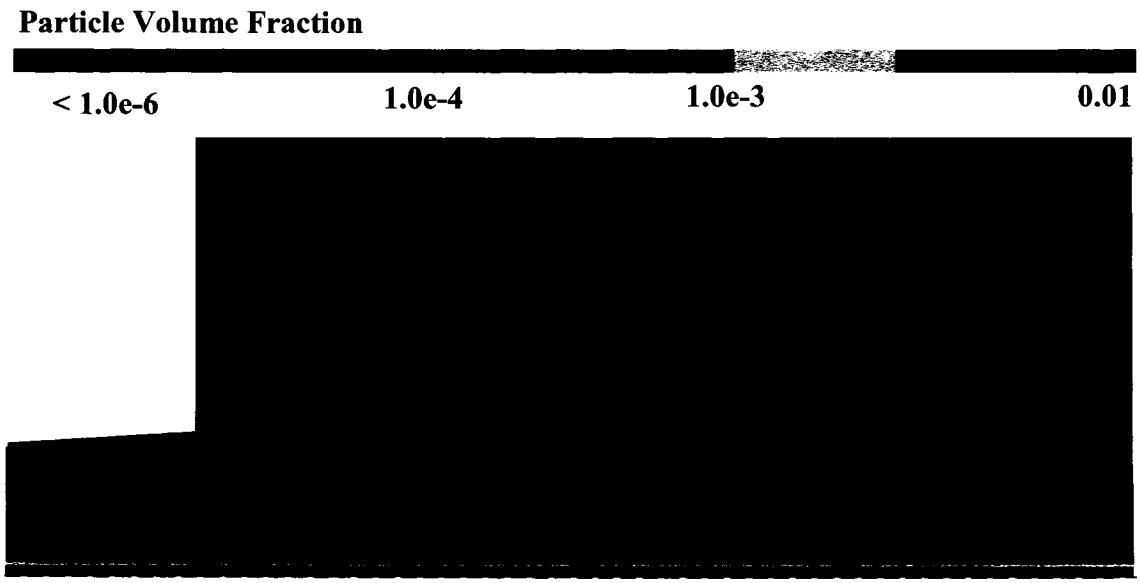

Figure 3.5: Particle volume fraction in a two-way coupled HVOF process

Gas phase velocity contours are chosen for study because gas velocity is an important characteristic which accelerates the particles by exchange of momentum. *Figures 3.6 (a)* and *(b)* show the velocity contour of the gas phase before and after particle injection, respectively; particles are injected at a bench mark loading of around 10 g/min (The corresponding volume fraction of particle phase is in the order of $2.e^{-4}$, approximately). By comparing the figures, it can be observed that the injection of particles, even though at a very small flow rate, changes the pattern of the shock diamonds that are formed outside the nozzle exit.

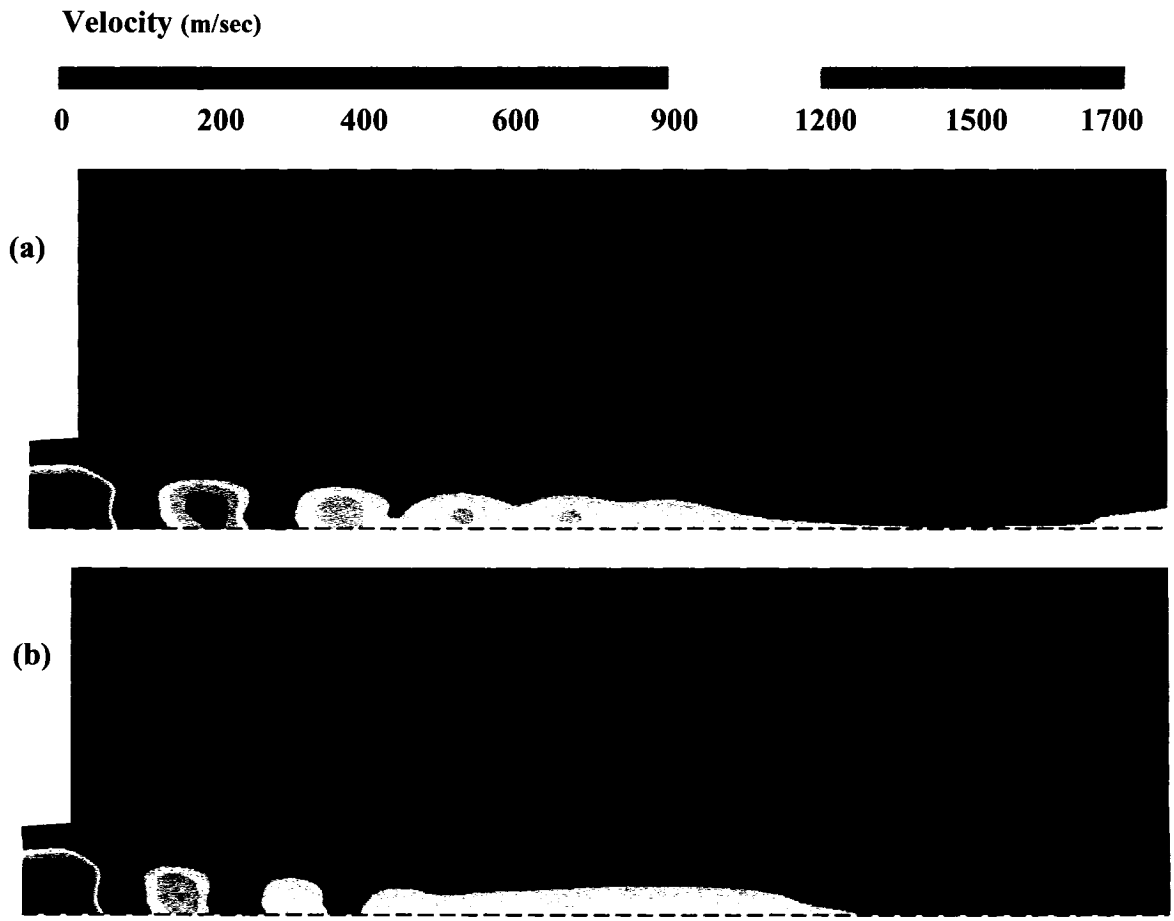

Figure 3.6: Gas phase velocity contour (a) before particle injection (single phase scenario) (b) after particle injection at a loading of 10 g/min

Close examination of *Figure 3.6 (b)* would reveal that the strength and number of shock diamonds is reduced when particles are injected. In addition to this we can see that the shocks are slightly shifted away from the nozzle centerline and there is a slight reduction in the gas velocity in that region, as well. This is due to the presence of the particle phase near the nozzle centerline, although not very dense in volume fraction. Away form the nozzle centerline, it can be seen that the flow characteristics are almost similar before and after particles injection. This gives a very clear picture about the effect of loading in a two-way coupled dense two-phase flow. In order to study further the effect of loading, the particles are injected at various mass flow rates and the effect of this loading variation on the gas phase velocity are presented in *Figure 3.7*.

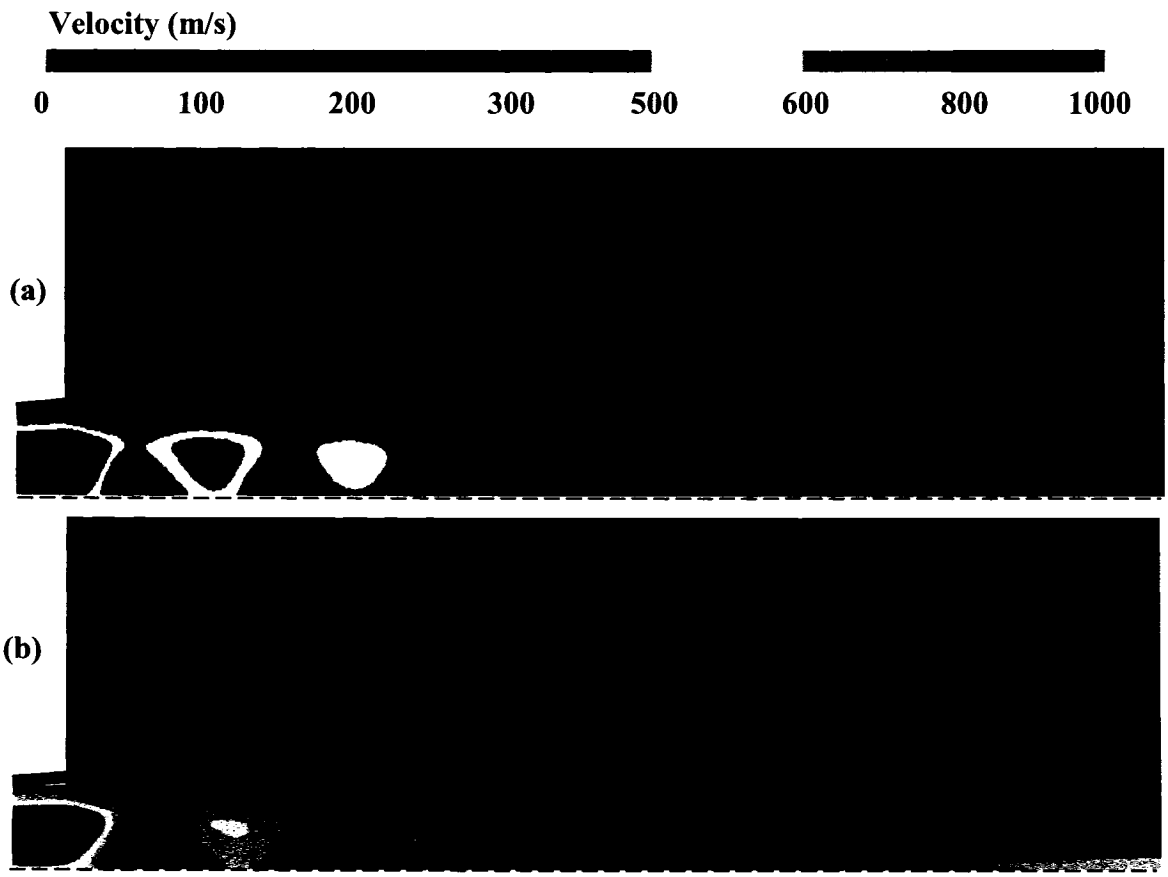

Figure 3.7: Gas phase velocity contour with different loading (a) 50 g/min (b) 150 g/min

Figure 3.7 shows the comparison of the gas phase velocity contours, when particles are injected at two different mass flow rates, namely 50 and 150 g/min. By increasing the particle loading, there is a significant change in the gas phase velocity. First of all the, the maximum gas phase velocity at the nozzle exit is drastically reduced to almost 1000 m/s, which is just little more than half of the velocity attained, if no particles were injected. Additionally the shock diamonds appear to be very weak and are shifted away from the centerline (where the particulate phase is dense) of the nozzle; number of shock diamonds is also reduced with increase in the particle loading. From the *Figures 3.6* and *3.7*, it can be inferred that an increase in particle loading would severely decelerate the gas phase velocity, which plays a major role in the delivering particles on the substrate.

Investigation of gas velocity variations across the nozzle exit plane would reveal the effect of particle volume fraction in a two-phase flow, ranging from dilute to dense. *Figure 3.8* demonstrates such an analysis. The axial velocity of the gas phase across the nozzle exit plane is plotted against the radial distance of the nozzle exit for different particle loadings. It can be visualized from the figure that the single-phase gas velocity at the nozzle wall is zero, after which the gas velocity across the plane increases and reaches its maximum at the centerline. When particles are injected at a loading of 10 g/min, the velocity of the gas near the centerline reduces to 1100 m/s, although the velocity of the main stream is around 1400 m/s. Upon increasing the particle loading to 50 g/min the gas velocity near the centerline drops to around 700 m/s with the main stream velocity descended to slightly above 1000 m/s. This shows that when particle loading increases, the gas velocity is not only affected near the centerline, but also globally.

In practical scenarios loading is not exceeding 100 g/min, but to show the consequence of particle loading, particles are overloaded at the rate of 150 and 400 g/min. It can be seen that when particles are overloaded with 150 g/min, the velocity of the main stream reduces down sharply to around 800 m/s with local velocity near the centerline less than 600 m/s. With the gas temperature close to 1600 K in this region, the flow regime is clearly subsonic near the nozzle centerline. This is why the shock diamonds are shifted away from the centerline, which is otherwise present in a single phase flow. It can be inferred that when particle loading is 400 g/min, the gas flow is subsonic globally.

The subsonic nature of the gas phase at higher particle loading is clearly shown in *Figure 3.9*, where gas phase Mach number along the nozzle centerline is plotted against axial

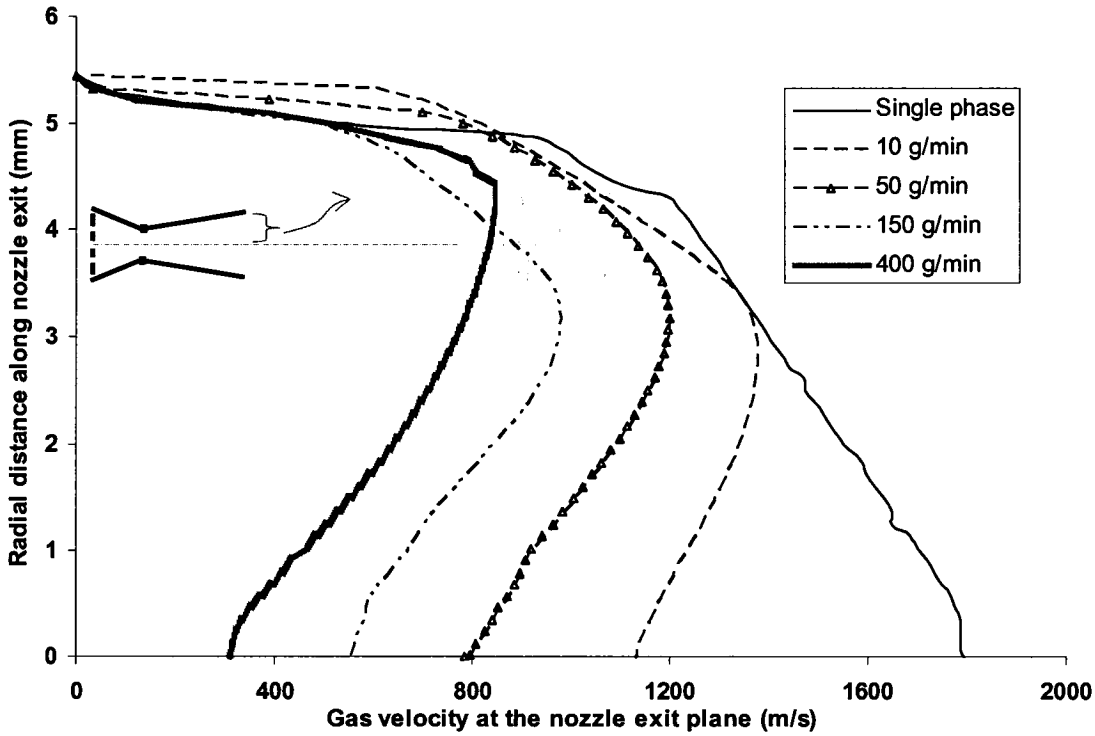

Figure 3.8: Gas velocity across the nozzle exit plane for different particle loading

distance. For simplicity, the Mach number is plotted for axial distance between nozzle throat and 14 cm from nozzle exit. It is evident from the figure that at a particle loading of 10 g/min the gas phase Mach number at the nozzle exit is around 2.1, whereas at a loading of 50 g/min the Mach number comes down to around 1.5. At the same loading rate the gas Mach number is supersonic at an axial distance of 12 mm, (i.e. at 5 mm from nozzle exit) whereas at a high loading of 150 g/min, the Mach number at exit is slightly above 1 which becomes subsonic shortly thereafter. When particles are overloaded (at 400 g/min) it can be seen that the gas Mach number is less than 0.5 at the throat and thus it does not even reach supersonic velocity at any point of the flow regime.

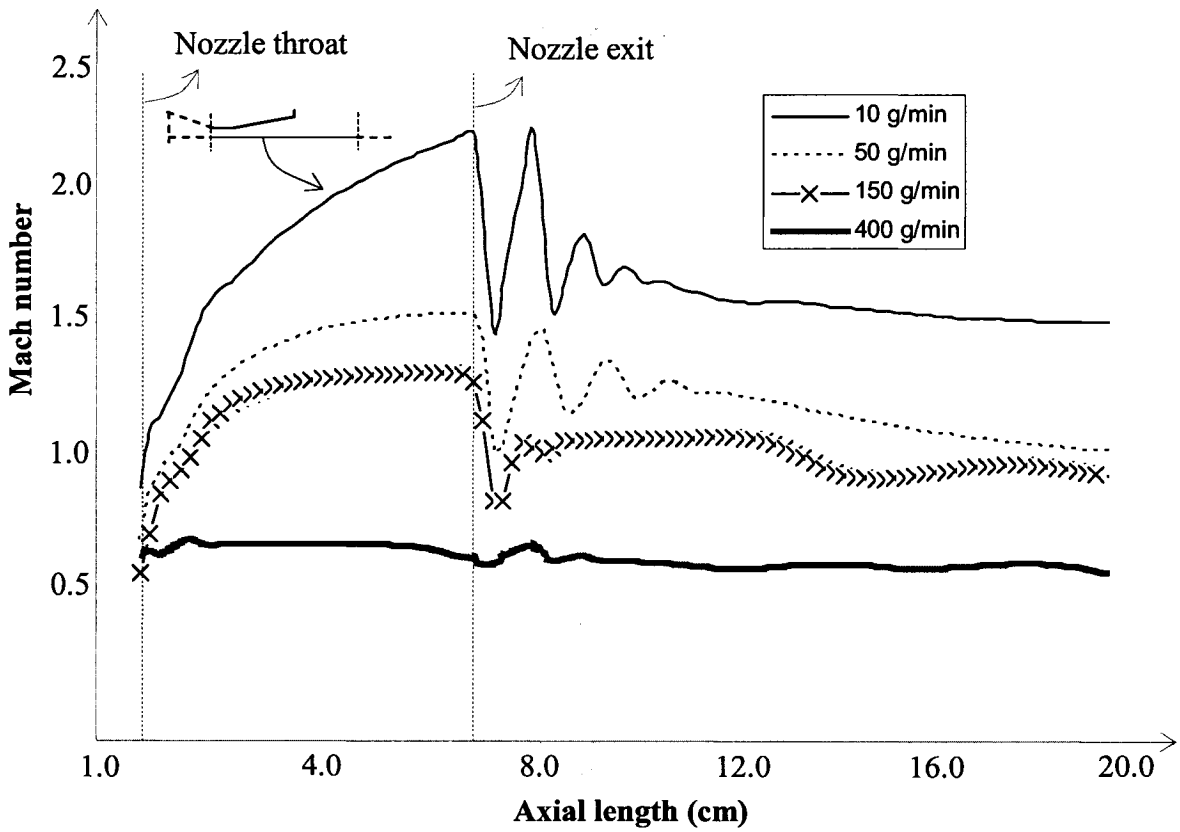

Figure 3.9: Gas phase Mach number across centerline for different particle loading

At this stage it is appropriate to refer *Figure 2.1*, which explains the relationship between drag coefficient and relative Mach number. From the figure it can be inferred that for high Reynolds number flow, as in HVOF process, the drag coefficient drastically increases to 4 for relative Mach number (which depends on relative velocity between gas and particles) is more than 1.2, whereas it is less than 0.5 for lower relative Mach number. When the Mach number of the gas phase is very low (i.e. subsonic) it directly affects the relative Mach number resulting in a low drag coefficient. Hence it is imperative to have supersonic flow regime as much as possible, which in turn depends on particle loading. This clearly shows the effect of particle loading on gas phase characteristics.

3.4.2. Effect of Particle Loading on Particle Phase

Particle acceleration in an HVOF process is due to the exchange of momentum with the gas phase. While the gas phase velocity playing a major role in momentum exchange, a descent of gas velocity due to high loading would definitely affect the momentum exchange thereby affecting the particle acceleration. *Figure 3.10* shows the effect of particle loading on particle velocity, where particle velocity along the nozzle centerline is plotted for various loadings. As mentioned earlier, the size of particles considered for this study is 30 μm; the particles are loaded at four different loading rates, namely 10, 50, 150, and 400 g/min. It can be seen that at different loadings, the same particles travel with different velocity. When the loading is very low i.e. at 10 g/min the particle velocity reaches 1200 m/s at the nozzle exit and thereafter it starts decelerating such that, at a distance of 250 mm from the nozzle exit the velocity is very close to 650 m/s. When the

particle loading is increased to 50 g/min, the gas phase acceleration is considerably reduced, which results in reduction of particle velocity. The particle velocities reaches a maximum of 550 m/s and thereafter the particles travel almost with the same velocity and finally when it reaches 250mm from the nozzle exit the velocity is around 500 m/s. By further increasing the loading to150 g/min and 400 g/min, particles velocity is very low velocity in the order of 450 m/s and 200 m/s, respectively.

It is very interesting to see that at the same stand-off distance of 250 mm, particles with same size have different velocities for different particle loadings. It can also be observed that the difference in velocity increases with a decrease in stand-off distance; say, at 200 mm from the nozzle exit, the particle velocity at loading 10 g/min is more than 700 m/s, while at a loading of 50 g/min, the particle velocity is close to 500 m/s. This gives

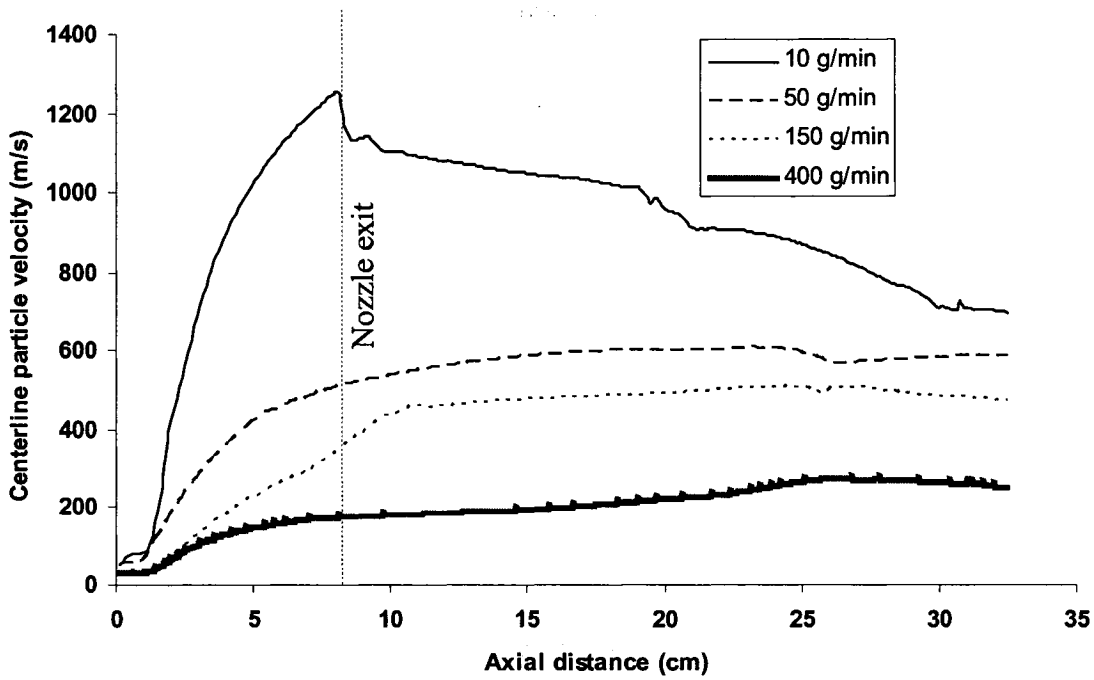

Figure 3.10: Particle velocity along the centerline for various loading

additional idea about locating substrate stand-off distance which is discussed in *section 2.3.4.* Thus it is seen that particle loading can considerably influence the velocity at which the particles are delivered on the substrate.

The intention of this chapter was to model a two-way coupled HVOF process, and to find the effect particle loading in dense two-phase flow. The next chapter will summarize all the major discussions of this work followed by scopes and recommendations where future research can be directed related to this work.

4. Closure

Computational modeling has been acknowledged as an important tool to study and understand complex phenomena such as gas-particle two phase flows, which finds application in a many natural and industrial systems. A High Velocity Oxygen Fuel coating process is numerically modeled and study has been done on various technological issues that are associated with this process. This thesis illustrates an HVOF process, which involves a complex particle-laden supersonic flow that operates at relatively high temperature. In addition to this various practical issues such as effect of a substrate on the flow field and particle loading are discussed in detail. The aim of this work is to study the intricacies and complexities involved in the HVOF process. Lagrangian and Eulerian approaches are applied to analyze the characteristics of the two-phase flow.

4.1. Conclusions

The first objective as mentioned in Chapter 1 was to model the HVOF process using the Lagrangian particle tracking method, assuming the particulate flow to be dilute and to investigate the characteristics of the gas phase and individual particles. In addition to this the presence of substrate in the flow field and its effect on the flowing particles is studied

for varying the substrate stand-off locations and substrate configurations. The results and conclusions of the Lagrangian approach are summarized as follows:

- The numerical simulation of the HVOF process, predicted wide range of flow properties such as gas pressure, temperature, density, velocity, Mach number, and species concentration. The simulation was also able to capture various flow characteristics such as abrupt temperature raise and hence the pressure raise due to the combustion, mixing layers, shocks diamonds, and flow dissipation by the turbulence. Numerical results showed good agreement with the experimental works conducted by Dolatabadi [37].

- Modeling combustion is one of the critical issues to accurately predict the flow characteristics in an HVOF process, as the results of combustion is the main source for the flow acceleration inside the nozzle. Combustion modeled using single step oxidation of propylene predicted unrealistically high temperature (about thrice the adiabatic flame temperature of propylene) and hence multi step combustion modeling was adopted, accounting for the intermediate chemical reactions. Care should be taken not to include unnecessary intermediate reactions, which would increase the computational time. In this work, a three step chemical reactions was considered and the results of combustion and concentration of various species show good agreement with experimental works.

- The properties of the particle phase were obtained by using the Lagrangian particle tracking approach. Using this method yielded the properties of individual particles in the flow field, such as particle temperature and velocity history. As drag coefficient plays an important role in the momentum transfer between the particles and the gas, suitable C_D correlation that accounts for a large range of Mach number and particle Reynolds number was used. The numerical results, especially the velocity of particles, obtained was slightly more than the experimental results obtained by Dolatabadi *et al.* [28] [37] and this over-estimation of velocity increases with increase in the particle size. The reason for this over-estimation of velocity may be due to the drag correlation, which raises the need to find a more appropriate drag model.

- The presence of shock diamonds at the nozzle exit was seen deflecting the particles from their respective trajectories and this is more pronounced for small sized particles. The shock diamonds did not have significant effect on particles with large diameter. In addition to this the presence of substrate in the flow field gives rise to strong bow shock or stagnation flow which strongly affects the particle conditions. This bow shock was found to be responsible for deviating particles with small size, while large particles showed poor response to the bow shock, due to their relatively large Stokes number.

- The strength of the bow shock was observed varying for various substrate stand-off distances. In order to understand effect of the substrate stand-off distance on

particle conditions, four different substrate distance were studied; 200, 250, 300, and 350 mm. Four different particle sizes namely 1, 10, 30, and 60 μm were injected and their conditions, mainly particle impact velocity and landing location, on the substrate were obtained. It was seen that impact velocity of smaller particles, in the order of 10 μm, on a substrate kept at 200 mm is relatively low due to the strong bow shock formed because of the flow impingement on the substrate thus shifting the average landing location far away from the nozzle centerline. The results also revealed that the particle sizes of 30 and 60 μm showed very similar pattern both in terms of impact velocity and landing location on the substrate.

- In order to clearly understand the effect of substrate configuration on the strength of the bow shock, general characteristics of gas phase in a free jet was compared with those of the flow impinging on three different substrate shapes; flat convex and concave. It was seen that the strength and nature of the bow shock changes significantly for different substrate configurations. To study the effect of the change in the substrate configuration on particle condition, two different particle sizes, namely 10 and 30 μm, were studied. These two sizes were chosen as they represent relatively small and large sized particles. It was seen that the presence of a flat substrate in the flow field decelerates the particle abruptly, deviating them from their trajectory. The bow shock formed on the surface of flat substrate was slightly stronger than that of the one formed on a convex substrate, thereby decelerating and deflecting the particles more near substrate. The bow shock was found to have least influence on 30 μm particles due to their large size, and hence large Stokes number.

- It was quite interesting to see that the bow shock formed on the concave substrate was much stronger than the bow shock formed on either flat or convex substrate. It was expected that the concave substrate would capture more number of particles due to their apparently favorable shape. On the contrary, due to the strong bow shock formed on this substrate, the 10 μm particles were severely decelerated and deviated, resulting in the escape of few particles without lading on the substrate. Even large sized 30 μm particles were found to be slightly affected by this strong bow shock.

- From the above analysis a conclusion can be drawn that if large particles can be used for coating, one can place the substrate either at 200 or 250 mm, depending upon the density and specific heat capacity of the coating particles. Placing the substrate nearer than 200 mm from the nozzle exit may result in the over-heating of the substrate due to the high temperature of the gas phase. If the substrate to be coated is either flat or concave, it is better to choose particle sizes close to 30 μm as they can easily travel undisturbed by either the shock diamonds or the bow shocks present in the flow field.

The second objective of this work was to apply Eulerian continuum method and to model a dense particulate phase scenario. In this analysis, as discussed in chapter 3, both the gas and particle phases were considered in an Eulerian frame and the effect of two-way coupling is studied by considering various particle volume fractions. The results can be summarized as follows:

- The High Velocity Oxygen Fuel process is simulated enabling a two-way coupling by using an Eulerian two-fluid model. Combustion is not modeled but appropriate boundary condition was given in order to create a high pressure and temperature at the nozzle inlet. Flow characteristics such as velocity, pressure, temperature, and in addition to these, the volume fraction of the gas phase were also obtained. The shock diamonds captured were not as sharp as those obtained using the Lagrangian model. This is due to the large mesh size used in the Eulerian simulation model that is necessary for the assumption of continuum for the particle phase. Due to the large mesh size, the maximum gas velocity predicted by the Eulerian method was underestimated.

- First the gas phase was modeled without injecting any particles and after convergence was reached, particles were injected at a bench mark flow rate of 10 g/min. Due to the effect of two-way coupling the injection of particles was found to be affecting the gas phase characteristics. It was observed that particle phase was dense in the region very close to nozzle centerline and dilute in the region away from the nozzle centerline. Due to this, the region where particle phase is dense, the gas velocity was found to be low, as it compares with the dilute particulate flow region. In addition to this, the strength of the shock diamonds appeared to be weak, with the shock diamonds slightly pushed away from the nozzle centerline. Number of shock diamonds was also found to be reduced.

- By increasing the particle loading rate to 50 g/min, it was observed that gas velocity near the nozzle centerline decreased significantly. Though the particle velocity increased radially away from the centerline, the maximum velocity of the free stream, i.e., away from the nozzle centerline where the particle phase is dilute, was also found to be reduced. Therefore, the Mach number of the gas was also found to be reduced, which results in subsonic flow immediately after the nozzle exit. This is the reason why shock diamonds were attenuated and the shocks were shifted away from centerline with lower strength. Further increase in the loading to 400 g/min, reduced the overall gas velocity considerably thereby changing the supersonic flow regime to subsonic for the entire computational domain.

- Increase in the particle loading results in the sharp descent of gas velocity, near the nozzle centerline, which directly affects the particle velocity. Particle velocity along the nozzle centerline, at different particle loadings was plotted and it was observed that the particle velocity at any given distance from the nozzle exit was different for different loadings along the centerline. For example, the particle velocity at a stand-off distance of 200 mm was close to 700 m/s at a particle loading of 10 g/min, whereas the velocity of the same particles at a loading of 50 g/min was close to 450m/s.

4.2. Recommendations for future work

Research in any particular field is never ending. There will always be a scope to increase the performance of outcome, which can be understood by continuing research in all possible sensible directions. This section is dedicated to give ideas and some recommendations for future work and some projects in pipeline as a continuation of current work. They are summarized as follows:

- There exist a mammoth amount of experimental data and result on HVOF process. However, not many of them discuss or give an insight about the presence of substrate in the flow field or the configuration of substrate. Therefore, the next and immediate project, as a continuation of present work is to experimentally study the effect of substrate and effect of its configuration.

- Working on various nozzle configurations is also in the pipeline. Joshi *et al.* [43] have studied the nozzle orientation effects of nonlinear interactions on exhaust supersonic jets and have predicted that a rectangular nozzle exit would considerably decrease the atmospheric air entrainment into the main jet that emerges out of the nozzle. Decrease in the air entrainment into the main jet, would reduce the particle oxidation, which in turn would improve the coating quality [44]. Hence designing a nozzle with rectangular exit is one of the recommendations that can be done in the future.

- Extending the supersonic zone of the flow is one of the main steps that would increase the particle impact velocity, especially for smaller particles. Bauer *et al.* [45] have studied the effect of attaching a second throat at the nozzle exit, and it has been understood that such an attachment significantly improves the performance of the nozzle. Therefore such a second throat can be attached and examined to extend the supersonic domain of the flow.

This work finishes at this stage, after accomplishing the various objectives mentioned in *Section 1.7* namely investigating and comparing the HVOF process in Lagrangian method and Eulerian method, followed by the conclusions and recommendation for future work.

Reference:

[1] J. C. R. Hunt, *"Industrial and environmental fluid mechanics"*, Annual Review Fluid Mechanics, 23:1-41 (1991)

[2] C. T. Crowe, *"Review – Numerical models for Dilute Gas-Particle flow"*, Journal of Fluids Engineering Volume 104/297, (1982)

[3] C. T. Crowe, M. Sommerfeld, Y. Tsuji, *"Multi-phase Flows with Droplets and Particles"*, CRC Press, Washington, D. C., Chat 2, pp 25, 67.

[4] Liang-Shih and Chao Zhu, *"Principles of Gas-Solid Flows, Cambridge University Press, Cambridge"*, Chap 5, pp 164-165.

[5] Suzler Metco Ltd., Wohlen, Switzerland.

[6] D. B. Spalding, *"A General purpose computer program for multidimensional one and two-phase flows"*, Journal of Mathematical Computational Simulation Vol. 23 pp 267-276, (1981)

[7] B. Hassan, A. R. Lopez, W. L. Oberkampf, *"Computational Analysis of a Three-Dimensional High-Velocity Oxygen-Fuel (HVOF) Thermal Spray Torch"*, Proceedings of the 8th National Thermal Spray Conference, Texas (1995), pp 193 – 198.

[8] C. M. Hackett, G. S. Settles, *"The High-Velocity Oxy-Fuel(HVOF) thermal spray- Materials processing from a gas dynamics perspective"*, Fluid Dynamics Conference, 26th, San Diego, CA; UNITED STATES; 19-22 June 1995.

[9] C. M. Hackett, G. S. Settles and J. D. Miller, "*On the Gas Dynamics of HVOF Thermal Sprays, Thermal Spray Coatings: Research, Design and Applications*", C. C. Berndt and T.F. Bernecki, ED., ASM International 1993, pp 167-172.

[10] V. R. Srivatsan, Q. Zhu, A. Dolatabadi, *"Effect of substrate geometry on thermally sprayed coating particles"*, Proceedings of 17th International Symposium of Plasma Chemistry, (ISPC 2005), June 2005, Toronto, Canada.

[11] Q. Zhu, V. R. Srivatsan, A. Dolatabadi, *"Numerical Analysis of the effect of substrate in cold spray Process"*, Proceedings of 20th Canadian Congress of Applied Mechanics (CANCUM 2005), April 2005, Montreal, Canada.

[12] V. R. Srivatsan, A. Dolatabadi, *"Investigation of Particle-Shock Interaction in a thermal spray Process"*, Proceedings of 7th International Thermal Spray Conference (ITSC 2006), May 2006, Seattle, U.S.A.

[13] W Brandl, D Toma, J Kruger, HJ Grabke, and G Matthaus, "*Oxidation behavior of HVOF sprayed nano-crystalline NiCrAlY powder*", Surface and Coatings Technology, Switzerland, Volume 94-95, pp 21-26, 1997.

[14] S. M. Dash and R. D. Thorpe, "*Shock-Capturing model for one and two-phase supersonic exhaust flow*", AIAA Journal, Volume 19, pp 842-851, 1981.

[15] C. D. Donaldson and R. S. Snedekaer, *" A study of free jet impingement; Part 1 – mean properties of free and impingement jets"*, Journal of Fluid Mechanics, Volume 45, part 2, pp 281-319, 1971.

[16] C. D. Donaldson and R. S. Snedekaer, *" A study of free jet impingement; Part 2 – Free jet turbulent structure and impingement heat transfer"*, Journal of Fluid Mechanics, Volume 45, part 3, pp 477 - 512, 1971.

[17] G. D. Power, T. J. Barber, and L. M. Chiapetta, *"Analysis of High Velocity Oxygen Fuel (HVOF) Thermal torch"*, AIAA Paper number 1992-3598, SAE, ASME and ASEE, Joint Propulsion Conference and Exhibit, 1992.

[18] W. L. Oberkampf and M. Talpallikar, *"Analysis of a High Velocity Oxy-Fuel (HVOF) Thermal spray Deposition Torch;, Part 1: Numerical Formulation"*, Journal of Thermal Spray Technology, Volume 5 (No. 1), pp 53-61, 1996.

[19] W. L. Oberkampf and M. Talpallikar, *"Analysis of a High Velocity Oxy-Fuel (HVOF) Thermal spray Deposition Torch, Part 2: Computational Results"*, Journal of Thermal Spray Technology, Volume 5 (No.1), pp 62-81, 1996.

[20] B. E. Launder and D. B. Spalding, *"The numerical computation of turbulent flows"*, Computer methods in applied mechanics and Engineering, Volume 3 pp 269-289, 1974.

[21] N. Sinha, B. J.York, A. Hosangadhi and S. M. Dash, *"First principle-based Computational Fluid Dynamic (CFD) Model for Thermal Spray Deposition Process,* Proceeding of 8th National Thermal Spray Conference, Houston, Texas, pp 199-206 1995.

[22] X. Yang and S. Eidelman, *"Numerical Analysis of High-Velocity Oxygen-Fuel Thermal Spray system"*, Journal of Thermal Spray Technology, Volume 5, (No. 2), pp 175-187, 1996.

[23] B. Hassan, A. R. Lopez and W. L. Oberkampf, *"Computational Analyis of a Three-Dimensional High Velocity Oxygen-Fuel (HVOF) Thermal Spray Torch"*, Journal of Thermal Spray Technology, Volume 7, (No. 1) pp 71-77, 1198.

[24] V. V. Sobolev, J. M Gilemany, A. J. Martin, J. A. Calaero and P. Vilarrubais, *"Modeling of the in-flight behavior of stainless-steel powder particles in high velocity oxy-fuel spraying"*, Journal of Material Processing Technology, Volume 79, pp 213-216, 1998.

[25] A. Dolatabadi, J. Mostaghimi and V. Pershin, *"Effect of cylindrical Shroud on the Particle Conditions in High Velocity Oxy-Fuel Process"*, Science and Technology of Advanced Materials, Volume 3, pp 245-255, 2002.

[26] A. Dolatabadi, J. Mostaghimi and, M. Ivanovic, *"A fully Eulerian Approach to High Speed Particle Laden flows"*, Proceedings of 4th International Conference on Multiphase flows, New Orleans, LA, USA, 2001.

[27] A. Dolatabadi, J. Mostaghimi and V. Pershin, *"Interaction of shock and expansion wave with solid particles in supersonic flows"*, Proceedings of ASME Fluid engineering Division, Montreal, Canada, 2002.

[28] A. Dolatabadi, J. Mostaghimi and V. Pershin, *"Modeling Dense Suspension of Solid Particles in a Highly Compressible Flows"*, International Journal of Computational Fluid Dynamics, Volume 18 (No. 2), pp 125-131, 2004.

[29] V. R. Srivatsan and A. Dolatabadi, *"Particle-Shock Interaction in an HVOF Process"*, Journal of Thermal Spray Technology, December 2006

[30] B. F. Magnussen and B. H. Hjertager, *"On mathematical models of turbulent combustion with special emphasis on soot formation and combustion"*, Proceedings of the Combustion Institute, 1976.

[31] A. H. Lefebvre, *"Gas Turbine Combustion"*, Taylor and Francis, Philadelphia, USA, 1998, Chapter 1, pp 18.

[32] R. A. Strehlow, *"Fundamentals of Combustion"*, International Textbook Company, Scranton, Pennsylvania, 1968, Chapter 4, pp 77.

[33] C. Crowe and D. Stock, *"A Computer Solution for Two-Dimensional Fluid-Particle Flows"*, International Journal of Numerical Methods in Engineering, Volume 19, pp 185-196, 1976.

[34] M. J. Walsh, *"Drag Coefficient Equation for small particles in High Speed Flow"*, AIAA Journal, Volume 13, No. 11, pp 1526-1528, 1975.

[35] C. B. Henderson, *"Drag Coefficient of Spheres in Continuum and Rarefied Flows"*, AIAA Journal, Volume 14, No. 6, pp 707-708, 1976.

[36] Fluent by ANSYS Incorporated, Lebanon, New Hampshire, U.S.A.

[37] A. Dolatabadi, *"Ph.D. Thesis – A Computational Analysis of High Speed Particle-Laden Flows, Department of Mechanical Engineering and University of Toronto, 2002."*

[38] B. A. Kashiwa, *"Statistical theory of turbulent incompressible multi-material flow"*, Technical Report LA – 11088 – T, Los Alamos National Laboratory , 1987

[39] B. A. Kashiwa, N. T. Padial, R. M. Rauenzahn and W. VanderHeyden, *"A cell-centered ICE method for multi-phase flow simulations"*, Technical Report LA – UR – 93 – 3922, Los Alamos National Laboratory, 1994.

[40] B. A. Kashiwa and R. M. Rauenzhn, *"A multimaterial formalism"*, Technical Report, LA – UR – 94 – 771, Los Alamos National Laboratory, 1994.

[41] F.L. Addessio, J.B. Baugardner, J.K. Dukowicz, N.L. Johnson, B. A. Kashiwa, R.M. Rauenzahn, C. Zemach, *"CAVEAT – A Computer Code for Fluid Dynamics*

Problems with Large Distortion and Internal Slip", Technical Report, LA-10613-MS-REV.1, LANL, New Mexico, 1990.

[42] V. Casulli and D. Greenspan, "*Pressure method for numerical solution of transient, compressible fluid flows*", International Journal for Numerical Methods in Fluids, Volume 4, pp 1001 – 1002, 1984.

[43] Joshi R, Panickar P, Srinivasan K, and Raman G, *"Nozzle-orientation effects and nonlinear interactions between twin jets of complex geometry"*, Journal of Aircraft, AIAA Publications, vol. 43, no. 2, pp. 336-345, Mar-Apr 2006.

[44] A. Dolatabadi, J. Mostaghimi, V Pershin, *"High Efficiency Nozzle for Thermal Spray of High Quality, Low Oxide Content Coating"*, US Patent 6845929, March 2002.

[45] Bauer, R. C. ; German, R. C., *"The Effect of Second Throat Geometry On the Performance of Ejectors Without Induced Flow"*, AEDC-TN-133, 1961.